

# Poly(Vinyl Alcohol)/Poly(Acrylic Acid) Hydrogel in a dc Electric Field: Swelling, Shape Change, and Actuation Characteristics

Morshed Khandaker\*

Department of Engineering and Physics, University of Central Oklahoma  
Edmond, OK 73034, USA

\*mkhandaker@uco.edu

## Abstract

Poly(vinyl alcohol) (PVA)/Poly(acrylic acid) (PAA) hydrogel can be utilized as a biomimetic actuator and coating material for tissue-implant interface, when employing an electrical stimulus. The swelling, shape change, and actuation characteristics of PVA/PAA hydrogel in a range of dc electrical fields were determined to find the optimal electric field for the hydrogel application as biomimetic actuator and coating materials. The hydrogel samples were prepared by dissolving PVA and PAA in deionized water at 4 wt% and mixed together at 1:1 ratio. Two custom made experimental setups were fabricated; one used for the measurement of swelling ratio of the hydrogels; and the other used for the shape changes or actuation characteristics of the hydrogels. Swelling experiments show increased swelling ratios of the hydrogel due to 10 V, 20 V, and 30 V electric fields. The rate of increment of the swelling ratio of hydrogel samples under 10V was higher compare to those samples under 20 V and 30 V. The width and height changes of rectangular shapes and maximum deflection along the length of hydrogel sample due to a range of electric fields (0-30V) were measured using an optical microscope. Incremental shape change up to a specific threshold value (around 10V) was observed due to electric stimulus. Electrostatic actuation pressure of hydrogel samples under 10V was higher compare to those samples under 20 V and 30 V. These results suggested that optimal performance of PVA/PAA hydrogel can be achieved around 10V.

## Keywords

*Poly Vinyl Alcohol; Poly Acrylic Acid; Ionic Hydrogel; Swelling Effect; Shape Effect; Actuation*

## Introduction

Ionic hydrogel is a copolymer of an N-substituted methacrylamide or acrylamide, a cross-linking heterogeneous agent [Luo *et al.*, 2007]. This polymer can deform elastically and can have equilibrium water content approximately 80%. Ionic hydrogels demonstrates a discontinuous volumetric change above

a specific threshold of an external stimulus such as pH, temperature, ionic strength or concentration of organic solvent. Structural support and controlled shape for the swelling hydrogel can be achieved by such ionic hydrogel. The volume, shape and deflection changes of the ionic hydrogel can be utilized for the fabrication of micro or nano scale actuation devices, which mimics the conversion of chemical or electrical energy into mechanical energy. Researchers have developed such actuator based on rapid electric field-associated bending deformation of a cross-linked hydrogel of poly(vinyl alcohol) chains entangled with poly(acrylic acid) [Dumitriu, 2001]. PVA/PAA hydrogel is an ionic hydrogel that changes shape when placed under an electrical stimulation [Jabbari *et al.*, 2007].

The tissue-biomaterial interface is the weakest place in the grafted hard-soft tissues interfaces such as bone-cement [Khandaker *et al.*, 2011]. Little research has been conducted on enhancing the integration of hard-soft engineered tissue scaffolds. A strong interface between a biomaterial and the surrounding tissue is integral to an artificial graft's functionality and long-term performance. Presuming this interface can be strengthened, it would have great medical applications. Tissue-biomaterial interfaces made with nano surface roughness and physically stimulated biomaterials may enhance the cell dependent mechanical integration of the interfaces more than those interfaces made with nano smooth and physically non-stimulated biomaterials. It has been found that hydrogels that undergo mechanical deformation enhances osteoblast cellular attachment and proliferation [Toworfe *et al.*, 2010]. Small physical forces can enhance the tissue-biomaterial interface by increasing the chondrocyte densities at the interface of tissue-biomaterial constructs. Lu *et al.* [Lu *et al.*, 2009] investigated a new approach for improving the electrode-neural tissue

interface. PVA/PAA hydrogel were used for coatings for poly-(dimethylsiloxane) (PDMS) based neural electrodes with the aid of plasma pretreatment. This study suggested that the hydrogel coating is feasible and favorable to neural electrode applications.

The major goal of our study was to examine whether enhanced tissue-biomaterial interface can be achieved by PVA/PAA hydrogel as a coating material for the implant at the tissue-implant interface. To achieve this goal, the specific aims for this study were: (1) to measure actuation force of the electric stimulus controlled PVA/PAA hydrogel, (2) to determine if the actuation force of the PVA/PAA hydrogel is affected by the swelling and shape characteristics of the hydrogel, and (3) to determine the optimal electric field for the hydrogel application as micro actuator or tissue-implant interface.

## Materials and Methods

### Specimen Preparation

Polyvinyl alcohol (PVA) and polyacrylic acid (PAA) were purchased from Sigma Aldrich and used without further purification. PVA was 89% hydrolyzed polyvinyl acetate and had a Mw of 146–186 kDa. PAA that contains less than 0.5% benzene having a Mw of 450 kDa and Tg of 106°C. The PVA/PAA hydrogel samples were prepared by dissolving PVA and PAA in deionized water at 4% and mixed together at a 1:1 ratio according to Quintero *et al.* [Quintero *et al.*, 2010]. The hydrogel was dehydrated in a custom made aluminium well plate in VWR iso-temperature oven (Sheldon Manufacturing Inc., Cornelius, OR) at 60°C for at least 24 hours.

### Design and Manufacture of the Setup and Instrumentation

Two experiment setups were fabricated in this study, one of which was used for the measurement of swelling of the hydrogel; while the other for the measurement of shape and actuation characteristics of the hydrogel. Each setup used True Energy 9.6V/1600mAh Ni-MH RC car battery (purchased from RadioShack Corp.) for the supply of constant dc voltage. An electronic circuit having linear regulator was created to control the voltage supply. For swelling experiment as shown in Fig. 1, a bath was fabricated using dimension elite 3D printer (Dimension Inc., Eden Prairie, MN). The bath has two slots for platinum plated titanium mesh anode (1/2" x 4" size with a 3" lug) and cathode (2"x6"size with 3" lug) electrodes. The electrodes were purchased from Rolling Thunder

Pyro Corp., Rhinelander, WI. The dimension of the bath in the setup is suitable to fit a tissue culture 24 well plate (BD Falcon). Multiple swelling experiments can be conducted using this setup.

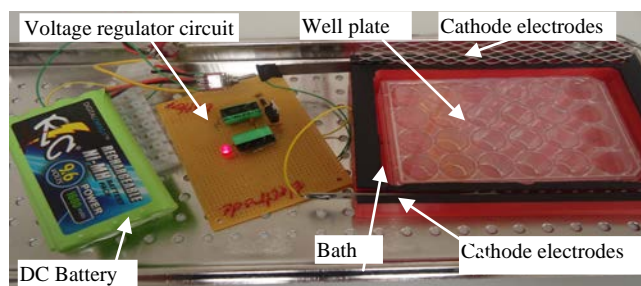


FIG. 1 EXPERIMENTAL SETUP FOR SWELLING TESTS.

For shape characteristics experiments as shown in Fig. 2(a), two bath chambers with common slots for the platinum anode/cathode electro sets were fabricated using dimension elite 3D printer; one for height measurement and the other for width measurement. Each bath has a rectangular slot in the middle to latch a hydrogel holder as shown in Fig. 2 (b). The holder has serrated clamp to secure a rectangular shape hydrogel sample. Nikon SMZ stereomicroscope was used to measure the height and width changes. For actuation characteristics experiments, a plastic sheet that acted as a reference bar was glued with the holder by cyanoacrylate adhesive. The bath was placed on the XY stage for microscopic viewing purpose.

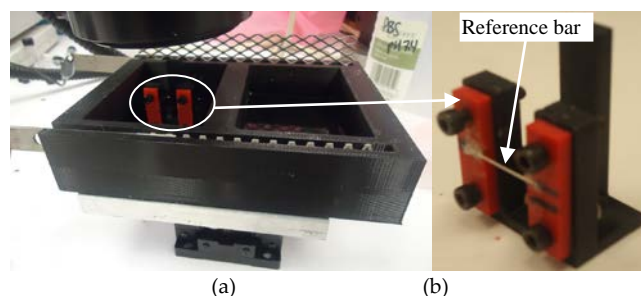


FIG. 2 EXPERIMENTAL SETUP FOR SHAPE CHANGE AND ACTUATION TESTS.

### Measurement of Swelling Characteristics

For swelling studies, approximately 20 mm × 20 mm size hydrogel samples were cut from the dried hydrogel films by a scissor. The samples were placed in at least 100 ml of phosphate buffer solution (PBS) in cell culture flask. The hydrogel was weighed before swelling and then pre-swollen for at least 24 hours. The swelling ratio was calculated by the swelling ratio equation as follows [Kim *et al.*, 2004]:

$$\text{Swelling Ratio} = \frac{w_f - w_i}{w_i} \times 100\% \quad (1)$$

where  $w_f$  is the mass after the electric field and  $w_i$  is the

initial mass before swelling.

**Measurement of Shape Change Characteristics**

A rectangular shape fully swollen hydrogel sample with dimension of 10 mm × 5 mm was cut out, secured in the specimen holder, and placed in a fabricated bath as shown in Fig. 2(a) at 10 V, 20 V, and 30 V for 2 hours. The dimensions of the height and width were measured every 10 minutes. Nikon SMZ 1000 stereo microscope was used to record the width and height changes in the hydrogel due to the electric field. Since the sample were secured using a clamp at the two ends, therefore, the length stayed constant. The dimension and shape changes of the samples from the recorded video were measured by Nikon NIS element basic research software as shown in Fig. 3 (a) and (b). The deformation ratio (contraction/expansion) of a sample was calculated from the following equation:

$$\text{Deformation ratio (\%)} = \frac{L_t - L_o}{L_o} \times 100 \quad (2)$$

where  $L_o$  and  $L_t$  are the initial and incremental height/width of the fully swollen sample in the various buffered solutions and length of the sample at a time,  $t$ , respectively.

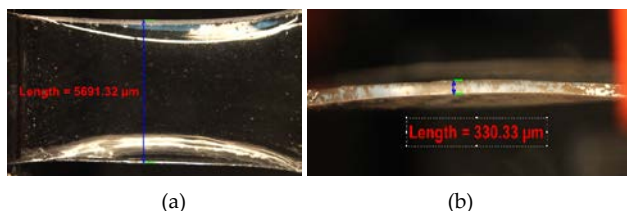


FIG. 3 MICROSCOPIC IMAGE OF DIMENSIONS OF A PVP/PAA SAMPLE: (a) HEIGHT AND (b) WIDTH

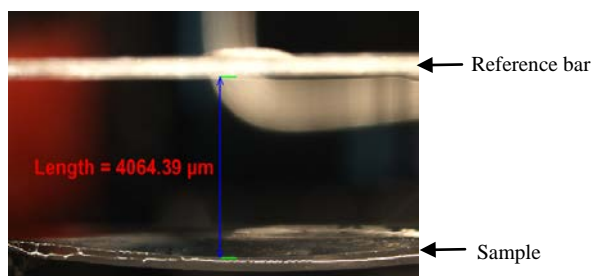


FIG 4. MICROSCOPIC IMAGE FOR THE MEASUREMENT OF MAXIMUM BENDING DISPLACEMENT OF A PVP-PAA SAMPLE FROM A REFERENCE BAR.

**Measurement of Actuation Characteristics**

The recorded video from a shape change experiment was used for the measurement of the maximum deflection of the hydrogel membrane. The maximum deflection of hydrogel membrane due to electric field was measured from the nonconductive reference bar as shown in Fig. 4. Electrostatic pressure was measured by Maxwell’s equation as follows [Shankar

et al., 2009]:

$$\text{Pressure, } P = \epsilon \epsilon_0 \left( \frac{v}{t} \right)^2, \quad (3)$$

with  $\epsilon$  is the permittivity of medium,  $\epsilon_0$  is the dielectric constant of the hydrogel,  $v$  is the applied voltage and  $t$  is the thickness of the sample. The values of  $\epsilon$  and  $\epsilon_0$  of an ionic hydrogel were assumed from literature [Luo et. al., 2007] as  $\epsilon = 80$  and  $\epsilon_0 = 8.854 \times 10^{-12} \text{ C}^2\text{N}^{-1}\text{m}^{-2}$ .

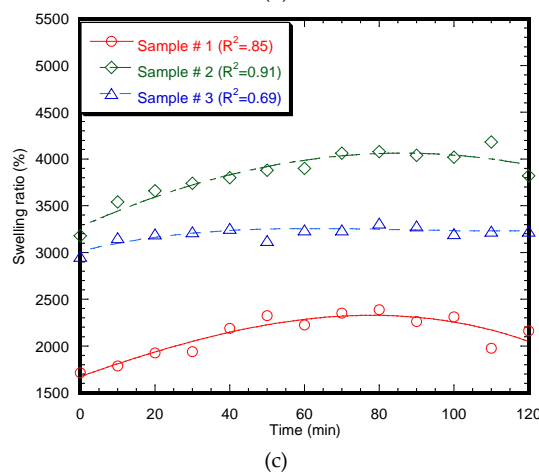
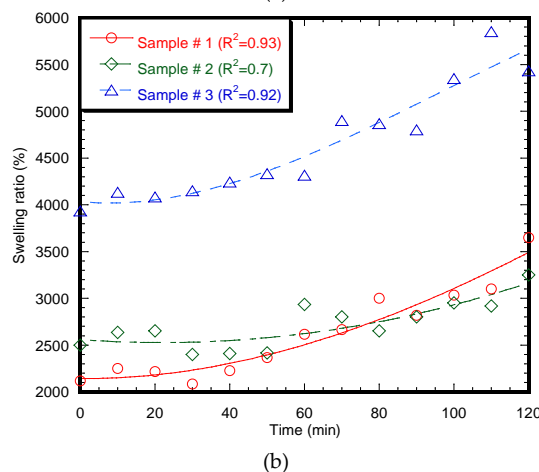
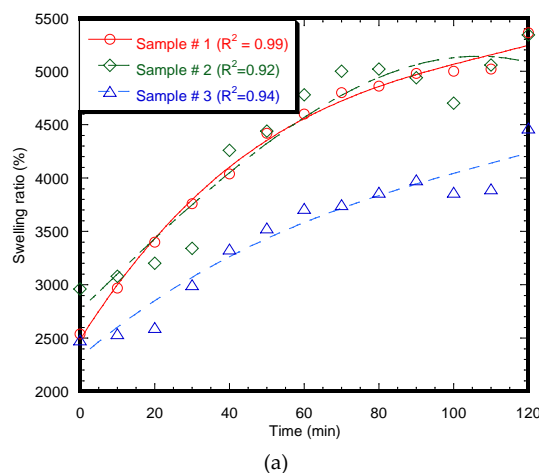


FIG. 5 THE VARIATION OF SWELLING RATIO UNDER (a) 10 V, (b) 20V, AND (c) 30V ELECTRIC FIELDS INTENSITIES VERSUS TIME. A 3<sup>RD</sup> DEGREE OF POLYNOMIAL FUNCTION WAS FITTED TO THE EACH SET OF DATA TO SHOW THE VARIATION.

## Results and Discussion

### Swelling Characteristics:

Fig. 5 shows the swelling kinetics and time dependent swelling behaviour of the hydrogels in water at 10 V, 20 V, and 30 V. The hydrogels incrementally swelled for all 10 V, 20 V and 30 V electric fields. Although the increase of swelling ratios of all three samples tested under 10 V were higher than those sample under 20 V and 30 V. The swelling ratios of all three samples tested under 30 V were lower than those tested under 20 V. The sample at 10 V exhibited the highest rate of swelling ratio for the time dependent swelling behaviour, while the sample at 30 V exhibited the lowest rate of swelling ratio. The hydrogels also showed distinct voltage dependent swelling behaviour in pure water. The data of swelling ratio and time for all electric fields were fitted by a 3rd degree polynomial function. The polynomial function of swelling ratio versus time under 10 V and 30V electric field intensities was concave, whereas a convex polynomial function was found for the 20 V electric field intensity.

### Shape Characteristics:

Fig. 6(a) shows the discontinuous changes of heights for the rectangular shape hydrogels measured in a PBS solution in continuous applied electric field ranges from 0-30V values. The constant applied electric field across two the parallel platinum electrodes caused a contraction of the PVA-PAA hydrogels in the buffered solutions at higher voltages. The contraction increased proportionally with the increase of voltage. The contraction of the hydrogels showed a higher width change after 20 V. Fig. 6(b) shows the change of width for rectangular shape hydrogels measured in PBS solution in an applied electric field ranging from 0-30V values. The constant applied electric field across the two parallel platinum electrodes caused an expansion of the PVA-PAA hydrogels in the buffered solutions at higher voltages. The expansion increased proportionally with the increase of voltage until 10 V. The expansion of the hydrogels showed a gradual decrease after 10 V. The ratio of expansion of width was significantly higher than the ratio of contraction of height. The resultant incremental shape changes occurred due to the increased swelling ratio behavior and ionic motion of the hydrogel at higher voltages. An increase in water absorption on one hand caused large swelling and mechanical instability of the coatings on the sample; on the other hand it enhanced

electrical signal transfer across the electrode interface by offering high ionic conductivity near the electrodes [Lu *et. al.*, 2009].

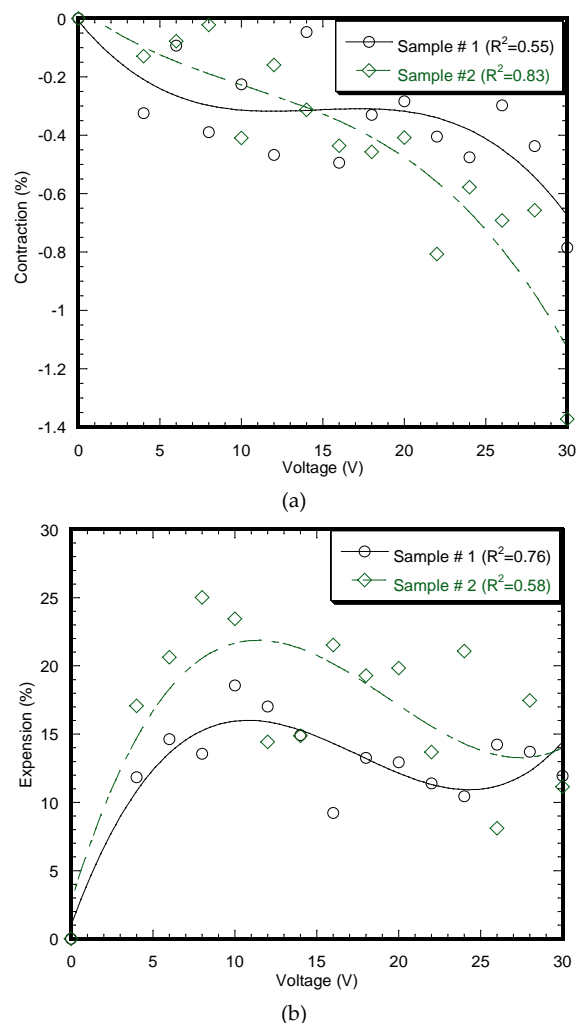


FIG. 6 THE VARIATION OF DIMENSION CHANGES OF (a) HEIGHT AND (b) WIDTH FROM 0 TO 30V ELECTRIC FIELD INTENSITIES. A 3<sup>RD</sup> DEGREE OF POLYNOMIAL FUNCTION WAS FITTED TO THE EACH SET OF DATA TO SHOW THE VARIATION.

### Actuation Characteristics

Fig. 7 (a) shows the variation of maximum displacement under 10 V, 20 V, and 30V electric field intensities versus time. Uniform deformation after a specific threshold time interval (50 to 60 minutes) was observed due to electric stimulus. Results showed that the deflection of hydrogel under 10 V and 20V was higher compared to the deflection of those hydrogel under 30 V. Additionally, the deflection-time functions of hydrogel at 10 V and 20 V were significantly different compared to the deflection-time functions of those hydrogel samples at 30 V. Fig. 7(b) shows the calculated electrostatic actuator pressure versus deflection at the 50th minutes test time for 10 V, 20 V,

and 30 V. Results showed that lower electrostatic pressure or internal stress and higher deflection or internal strain is generated in the hydrogel at higher voltages compared to the smaller voltages, when the samples were under a continuous electric field. The result also shows that the applied electric field produces negative stiffness to the hydrogel. This happens because of higher swelling ratios of hydrogel samples at higher voltages. The larger swelling expands the structure of the porous network in the hydrogel that leads to internal deformation.

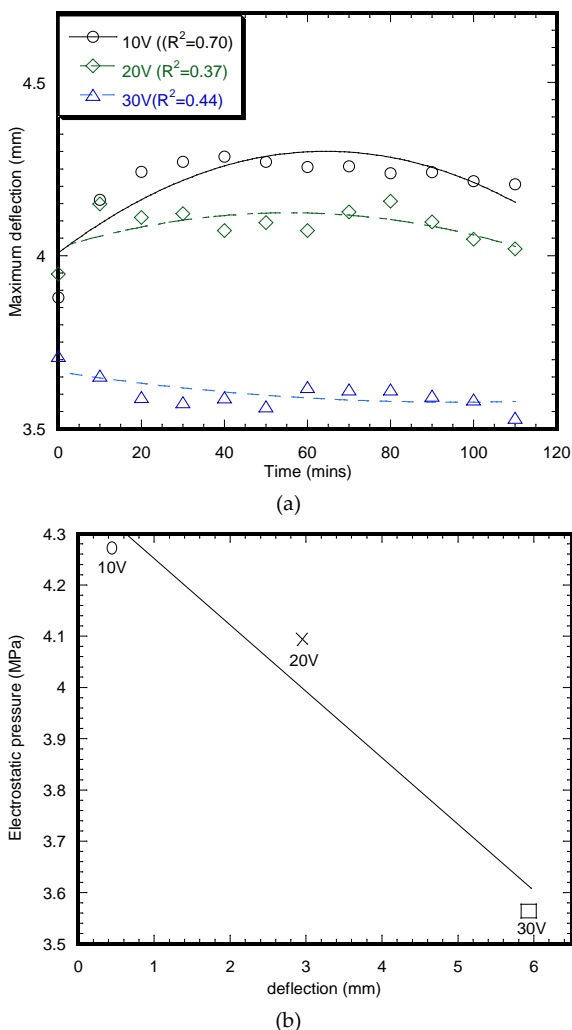


FIG. 7 (a) THE VARIATION OF MAXIMUM DISPLACEMENT UNDER 10 V, 20V, AND 30V ELECTRIC FIELD INTENSITIES VERSUS TIME. A 2<sup>ND</sup> DEGREE OF POLYNOMIAL FUNCTION WAS FITTED TO THE DATA TO SHOW THE VARIATION. (b) THE VARIATION OF ELECTROSTATIC PRESSURE VERSUS MAXIMUM DISPLACEMENT CALCULATED AT THE 50TH MINUTE OF THE EXPERIMENT FROM A PVP-PAA SAMPLE. A LINEAR FUNCTION WAS FITTED TO THE DATA TO SHOW THE VARIATION.

## Conclusions

Couple of experimental set ups were successfully

designed and fabricated for determining the swelling ratio, shape change characteristics, and deflection due to electrostatic force. The purpose of characterizing the PVA/PAA hydrogel was to determine whether the volume change of the PVA/PAA hydrogel can be utilized as coating material for tissue-implant interface and to determine the optimum voltage for the application. The graphs show that with an increase of voltage, there is an increase in swelling and volume change. The increasing trend of swelling and volume of the hydrogel leads to higher deflection. The deflection of the hydrogel showed a decrease of electrostatic pressure with an increase in voltage. The PVA/PAA hydrogel generates incremental deflection with reduced internal stress due to the electrical stimulus. Further application of the PVA/PAA hydrogel for tissue-implant interface is currently undergoing.

## ACKNOWLEDGMENT

This publication was supported by Grant Number P2PRR016478 from the National Center for Research Resources, a component of National Institute of Health (NIH) and CURE-STEM faculty scholar award support from University of Central Oklahoma (UCO). The authors would like to thank Miss Kelli Duggan for her help in specimen preparation and testing.

## REFERENCES

- Dumitriu, S., *Polymeric biomaterials*: CRC Press, 2<sup>nd</sup> Edition, 2001.
- Jabbari, E., Tavakoli, J., and Sarvestani, A. S., "Swelling characteristics of acrylic acid polyelectrolyte hydrogel in a dc electric field," *Smart Materials and Structures*, vol. 16, pp. 1614-1620, 2007.
- Khandaker, M., Li Y., and Tarantini, S., "Interfacial fracture strength measurement of tissue-biomaterial systems," in 2011 ASME International Mechanical Engineering Congress and Exposition. Denver, Colorado, 2011.
- Kim S. J., Kim Ii, H., Park, S. J., and Kim S. I., "Shape change characteristics of polymer hydrogel based on polyacrylic acid/poly(vinyl sulfonic acid) in electric fields," *Sensors and Actuators, A: Physical*, vol. 115, pp. 146-150, 2004.
- Luo R., Li H., and Lam, K. Y., "Coupled chemo-electro-mechanical simulation for smart hydrogels that are responsive to an external electric field," *Smart Materials and Structures*, vol. 16, pp. 1185-1191, 2007.

- Lu Y., Wang D., Li T., Zhao X., Cao Y., Yang H., and Duan Y. Y., "Poly(vinyl alcohol)/poly(acrylic acid) hydrogel coatings for improving electrode–neural tissue interface," *Biomaterials*, vol. 30, pp. 4143-4151, 2009.
- Quintero, S. M. M., Ponce F, R. V., Cremona, M., A. Triques, L. C., d'Almeida, A. R., and Braga, A. M. B., "Swelling and morphological properties of poly(vinyl alcohol) (pva) and poly(acrylic acid) (paa) hydrogels in solution with high salt concentration," *Polymer*, vol. 51, pp. 953-958, 2010.
- Shankar, R., Ghosh, T. K., and Spontak, R. J., "Mechanical and actuation behavior of electroactive nanostructured polymers," *Sensors and Actuators A: Physical*, vol. 151, pp. 46-52, 2009.
- Toworfe, G. K., Composto, R. J., Lee M. H., and Ducheyne, P., "Elastic membrane that undergoes mechanical deformation enhances osteoblast cellular attachment and proliferation," *International Journal of Biomaterials*, vol. 2010, pp. 1-10, 2010.

# Optical Emission Spectrometer, Principle and Latest Industrial Applications

Sumaira Nosheen<sup>\*1</sup>, Shahzad Alam<sup>2</sup>, Muhammad Irfan<sup>3</sup>, M. Usman Ali Qureshi<sup>4</sup>, Salman Ahmad<sup>5</sup>

Pakistan Institute of Technology for Minerals and Advanced Engineering Materials (PITMAEM)  
PITMAEM, PCSIR Labs Complex Lahore, Pakistan

<sup>\*1</sup>sumera\_pcsir@yahoo.com; <sup>2</sup>dg@pcsir-lhr.gov.pk; <sup>3</sup>enr.mirfan\_2007@yahoo.com; <sup>4</sup>engineerusman@gmail.com;

<sup>5</sup>Salman4431@yahoo.com

## Abstract

Optical Emission Spectrometer (OES) has become a valuable, versatile and universal equipment for the chemical analysis of metallic alloys. Typical parameter ranges include detection of 37 elements with 41 channels (for five bases including Fe, Cu, Zn, and Ni & Al). A high voltage spark/arc is used as a source for the excitation of sample in an inert environment. The radiations emitted by the sample are analyzed by PMT (photomultiplier tubes) acting as detector. Principle, working and the latest applications of the equipment are also discussed. Application of emission spectrometer in the field of production and fabrication, manufacturing areas, steel industry, surgical industry, auto industry and product development sector is also highlighted.

## Keywords

*Spectroscopy; Emission; Instrumentation; Radiations; Dispersion Order; Metallic Alloys*

## Introduction

Atom emission spectroscopy is, today, the backbone of chemical analysis for the identification, specification and process control in virtually all branches of the metallurgical industry. Optical Emission spectrometer provides a non-evasive probe to investigate atoms, ions and molecules within plasma. Emission spectroscopy is the study of spectra. that are the light absorption, reflection and emission properties of matter. Emission spectroscopy helps to determine the chemical composition of metallic alloys, as well understand the inner working of atoms and sub atomic particles, study stellar evolutions and cosmic energy patterns. An optical Emission Spectrometer can be used to study the most basic structure of life (the molecule) and its inner working. It uses in surface engineering, the that are the light absorption, reflection and emission properties of matter. Emission spectroscopy helps to determine the chemical composition of metallic alloys, as well understand the inner working of atoms and sub atomic particles, study stellar evolutions and cosmic energy patterns.

An optical Emission Spectrometer can be used to study the most basic structure of life (the molecule) and its inner working. It uses in surface engineering, the semi conductor industry and analytical chemistry have enhanced knowledge in those fields and helped to develop new techniques in micro and macro engineering .

Arc emission spectrometers (also referred to as spark emission spectrometer) analyze metallic samples through the application of an electric arc or spark, causing analytes to emit light and thereby revealing their presence and concentration by distinct wavelength signature. A spark emission spectrometer provides spectral range as high as 780 nm.

Optical Emission spectrometry provides a non-evasive probe to investigate atoms, ions and molecules within plasma, as well as information about properties such as (excited state) species densities, electron-atom, atom-atom and ion-atom collisional effects, energy distribution of species, charge transfer between plasma constituents, and electric and magnetic fields to name a few.

In the production of unrefined metals from ore and in the process of alloy refining, emission spectroscopic analysis is very important. Significant progress has been made with automatic system including sample preparation both in laboratories and also on-site for rapid analysis of molten metal. Quality checks on outgoing semi-finished and finished products are carried out using stationary and mobile spectrometers. There are spectrometers systems within and at the end of the process.

## Working Principle

Every solid, liquid or gaseous substance appropriately excited emits different wavelength radiations which characterize the substance itself, or better they constitute its spectrum. Emission Spectrometer

identifies and quantifies emitted radiations and goes back to their chemical composition.

By spectroscopy, we usually mean experimental charting of the energy level structure of physical systems. For that purpose, the transition processes, spontaneous or induced among different energy states are studied and spectroscopy therefore normally means analysis of various types of radiation-electromagnetic or particle emission. Spectroscopic investigations can be of a fundamental or applied nature. In fundamental spectroscopy experimentally determined energy levels, transitions probabilities, etc are employed to obtain an understanding of the studied systems using adequate theories or models. Usually, certain primary quantities (wavelengths, intensities etc) are measured in spectroscopic investigations. These quantities are then used to evaluate more fundamental quantities. This process is schematically illustrated in figure 1.1. By investigating fundamentals the spectroscopic investigations can also be employed to go for applied studies i.e. in analysing materials for advanced industrial applications.

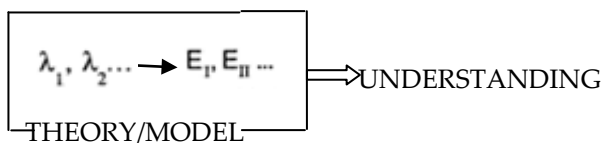


FIG. 1.1 THE SPECTROSCOPIC PROCESS

In principle, a set-up for spectral studies consists of three components: a radiation source, an analyzer and a detection system. In many modern techniques the system under investigation is subjected to different types of static or oscillatory fields and the influence of these fields on the system is studied in order to obtain a more complete picture of the system. Resonance methods are of special importance since they provide high accuracy in the determination of small energy splitting. The basic arrangement of a spectroscopic set-up is shown in Figure 1.2

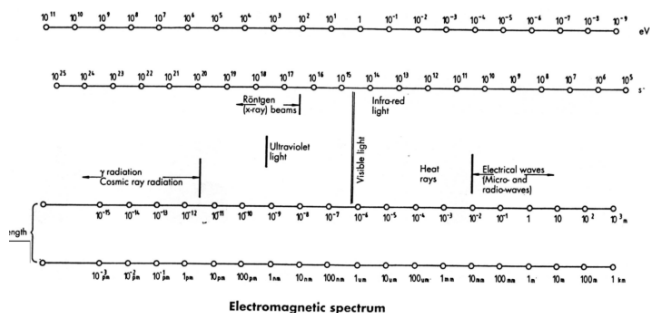


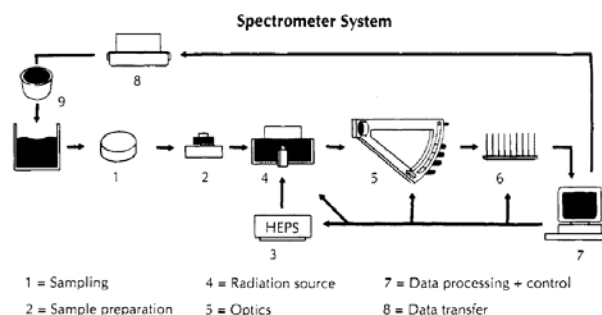
FIG. 1.2 ELECTROMAGNETIC SPECTRUM

Emission spectrometry is applied to almost every scientific and technical subject. Particularly, this

instrument is produced for metallurgy and generally for all activities based on complete Radiations emitted and absorbed by analyzed material are composed of electromagnetic field transversal oscillations which propagate as waves whose energy is not uniformly shared in the space, but it is clotted in well defined crumbs called quanta or photons.

TABLE 1 CONVERSION FACTORS BETWEEN ENERGY LEVELS

Unit	Joule	1 cm <sup>-1</sup>	Hz	eV
1 Joule	1	5.03378 × 10 <sup>22</sup>	1.50919 × 10 <sup>33</sup>	6.24150 × 10 <sup>18</sup>
1 cm <sup>-1</sup>	1.98658 × 10 <sup>-23</sup>	1	2.99792 × 10 <sup>10</sup>	1.23992 × 10 <sup>-4</sup>
1 Hz	6.62608 × 10 <sup>-34</sup>	3.33565 × 10 <sup>-11</sup>	1	4.13567 × 10 <sup>-15</sup>
1 eV	1.60218 × 10 <sup>-19</sup>	8.06502 × 10 <sup>3</sup>	2.41799 × 10 <sup>14</sup>	1



Atomic structure may be conveniently, even if not really, schemized in this way: in centre of the atom there is the nucleus, which contains almost the entire mass of the atom, but it occupies only one twelve-thousandth of the volume, instead the electrons move along nearly circular orbits around the nucleus.

Electrons instead are confined inside the atom because of the electromagnetic interaction between their charges (negative) and charges in the nucleus (positive). Energy by which electrons are bound in the atom is in the order of electron-volt (10<sup>-10</sup>eV), instead binding energy of the nucleons is in the order of MeV. If the atom receives energy at least equal to the binding energy of an electron, this one can leave the atom, which, lowered by a negative charge, remains positively ionized. However, inside the atom, electrons may occupy only well-defined orbits, each one characterized (being at different distance from the nucleus) by a different amount of energy. If an electron inside the atom is reached by a photon whose energy is exactly the difference of the binding energy between the level on which the electron is situated and an higher level (farther from the nucleus), the electron may jump in the excited level. An electronic configuration like that is not stable and all the electrons tend to go back to the fundamental level emitting the energy received just before, i.e. the energy equal to the "energy jump" between the levels.

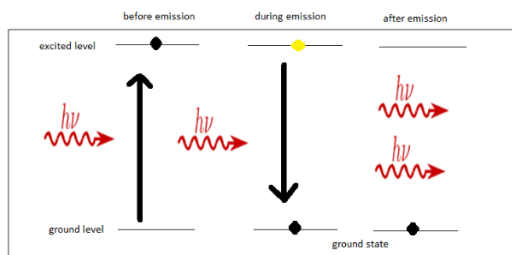


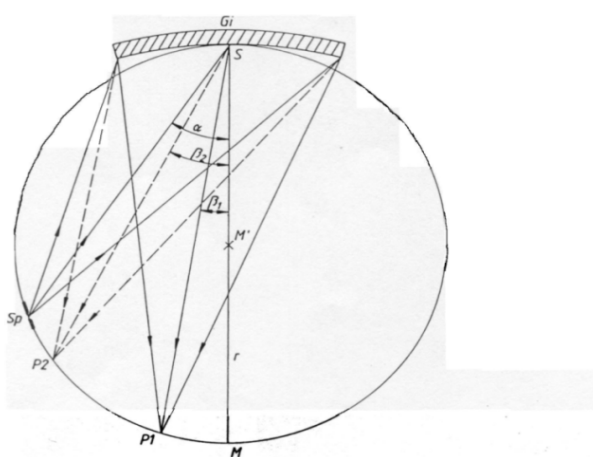
FIG. 1.5 SCHEMATIC DIAGRAM FOR SPONTANEOUS EMISSION  
 Considering atom belonging to different elements, even their electronic orbit structures are different and radiation emitted during de-excitation too.

Therefore knowing matter structure, analyzing emission spectra of a substance, i.e. observing emitted radiation wavelengths, we can recognize elements constituting the substance itself and, measuring these radiations intensities, as well evaluate the concentration of the element.

**Optical Emission Spectrometer**

**1) Instrumentation**

Optical emission spectrometer is 5-based system analyzing Copper, Iron, Nickel, Aluminum and Zinc based alloys. Metallic samples are prepared by grinding the surface with emery paper of grit size 2. The prepared sample is placed on the spark stand and a high voltage spark (900-1000 volts) is used as an excitation source.



Spectrometer optics with Rowland concave grating. Sp = Entrance slit; Gi = Grating; S = Apex; M = Centre point of circle; r = Radius of circle; P = Points in image plane

FIG. 1.6 SPECTROMETER OPTICS WITH ROWLAND CONCAVE GRATINGS

The entrance slit selects the part of radiation emitted by the sample which will join the grating. It is  $\approx 0.02$  nm in width and  $\approx 6$  mm in height. Dispersion that is separation of radiation in the monochromatic components is made by a concave grating. The grating is a dispersive means

characterized by very thin and equally-spaced lines engraved on a reflective surface. If the slit width and the distance between the lines have the same size order as incident radiation wavelength, the grating gives rise to dispersion that is separation of radiation to monochromatic components.

The refraction angle of any single monochromatic radiation, produced by the grating, is proportional to the wavelength of the radiation itself. Characteristics of holographic concave grating mounted on instrument are:

- Rules: 2400 rules/mm
- Range: 1400-4400 Å (extensible with special device)
- Bending radius: 750.2 mm
- Mounting: Paschen-Runge
- Blaze angle: 40°

Concave grating theory shows that if the entrance slit is on the circumference (Rowland Circle) having a diameter equal to the bending radius of the segment on which the grating has been laid out, maxima and minima of diffraction figure produced.

**2) Dispersion Orders**

In relation to monochromatic radiation, grating gives rise to many lines according to different diffraction orders. The angle equal and opposite to the angle formed by the incident ray and the normal determines the zero order. Therefore, at the same time, the grating gives not a single image of the spectrum, but many repetition of the same spectrum according to different diffractions orders of the wavelengths which form spectrum.

These features lead to the phenomenon of super imposition of different orders spectra, that is: first order diffraction angle of the  $\lambda$  corresponds to the second diffraction angle of the  $\lambda/2$  and to the third order angle of the  $\lambda/3$ . But respective intensities diminish.

**3) Exit Slits**

Every monochromatic image of the entrance slit is sharply reproduced on Rowland Circle. They consist in small photoengraved plates set on the circle. Their function is to isolate spectral lines belonging to the elements selected for the analysis allowing photomultipliers, situated immediately behind, to receive light coming out through the slits. Photomultipliers are put just behind the slits, if there is room enough, otherwise they are set elsewhere and radiation joins them by a mirror

system. Exit slits are 0.06 nm-009 nm in width, which is higher than entrance slit, to allow slight displacement of the spectrum without compromising radiation collection.

**Detector**

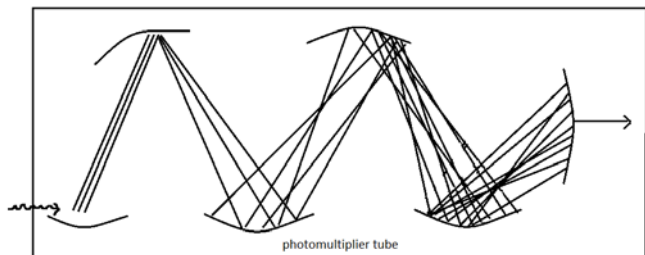


FIG. 1.8 PHOTOMULTIPLIER TUBE

**The Analysis**

Every analytical cycle of the spectrometer can be divided into three very well separated steps: flux, pre-discharge and exposition.

**1) Flux**

In this phase, lasting about 5 seconds, a stream of argon enters the excitation stand just before the discharge starts. Flowing argon keeps electrode and sample cleaned from impurities. Argon consumption during this phase is negligible.

**2) Pre-discharge**

This operation has two functions:

- 1) elimination of electrical defects (preferred points of attack by the discharge)
- 2) Remelting the sample in the burn spot and establishing the steady state.

Any sample produced under practical working conditions will have some defects (precipitates, cracks, holes), so that at the start of sparking more or less diffuse discharge will occur. The time required to eliminate the defects will become shorter with increasing discharge energy.

The remelting depth depends on conductivity and amounts to  $\approx 30-50 \mu\text{m}$  for pre-spark energy and  $10-20 \mu\text{m}$  for measurement energy during exposition; in fact during pre-sparking, the burn spot is larger than that during integration, thus ensuring that, during measurements, material is taken only from a region which has been remelted during pre-sparking to obtain homogenization.

The sparking-in time increases with the quantity and size of precipitates, and then declines with the energy converted per discharge, and it is completed when all precipitates and electrical defects in the sample surface have been removed.

The remelted quasi-structure with less layer grows with sparking time up to the steady state.

In the steady state, there is a quasi-structure having less layer present; and the composition of the sample in the burn spot region in the steady state is proportional to the mean composition of the sample. It is independent of the energy converted per discharge with which the steady state has been obtained.

During this phase, lasting about 20 seconds, the true analysis takes place. The points of the discharge attack are in the centre of the area previously burn by pre-spark that is discharges strike just homogenized area.

During exposition, the individual discharge must find identical preconditions: while during pauses between discharges the discharge space must be de-ionized.

During pauses between discharges the crater from the previous discharge must be cooled until there is no further thermal electron emission. If this is not the case, the following discharges will go to this crater position.

In practice, the best parameters and times of sparking and pre-sparking are not univocally fixed, because of, depending on sample elements, mutual interferences, bases, metallurgical history, the most effective conditions to get the steady state change.

Date: 09/26/11 11:49:16		Program: LAS											
Sample: ROD		Operator: Usman											
Ref. Alloy:		Analysis Mode: Standardized concentration											
	Fe %	C %	Mn %	P %	S %	Si %	Cu %	Ni %	Cr %	Mo %	Al %	Ti %	V %
1	98.539	0.132	1.007	0.013	0.016	0.240	0.001	0.004	0.008	0.001	0.015	0.026	0.000
2	98.520	0.124	1.010	0.011	0.016	0.247	0.001	0.002	0.007	0.001	0.028	0.033	0.000
3	98.521	0.134	1.006	0.014	0.016	0.241	0.001	0.004	0.002	0.001	0.023	0.039	0.000
Avg.	98.527	0.130	1.008	0.013	0.016	0.243	<0.001	0.003	0.006	<0.001	0.022	0.033	0.000
A.S.D.	0.0107	0.0053	0.002	0.0015	0.0	0.0038	0.0	0.0012	0.0032	0.0	0.0066	0.0065	0.0
	Co %	B %	Nb %	Zr %	Sn %	(-) W %							
1	0.001	0.000	0.000	0.001	0.000	0.001							
2	0.001	0.000	0.000	0.001	0.000	0.001							
3	0.001	0.000	0.000	0.001	0.000	0.001							
Avg.	<0.001	0.000	0.000	<0.001	0.000	<0.001							
A.S.D.	0.0	0.0	0.0	0.0	0.0	0.0							

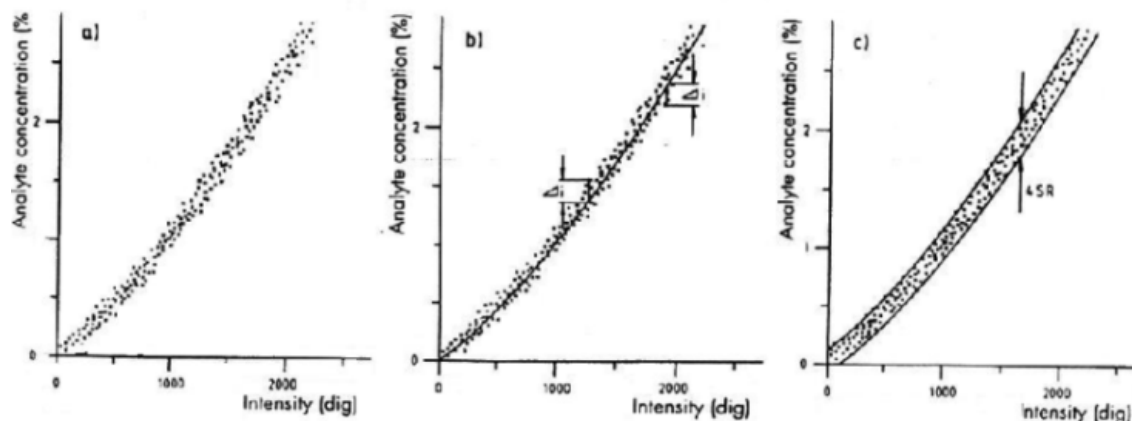


FIG. 1.9 CALIBRATION CURVES

For example, elements well dissolved in the base can be measured after sparking-in; and undissolved elements can be determined after their sparking equilibrium has been reached. If the metal has no precipitates, homogenization takes only a very short time, and pre-sparking lasts a few seconds, then the steady state is immediately reached.

The intensity must be measured in the steady state in cast sample with precipitates in varying forms and sizes because of inter-elementary effects, such as carbon on sulphur in steel.

### Results

The results are in the form of print out directly taken from the printer attached with the Software of Spectrometer.

### Calibration

After drawing on the plane concentration/intensity the points which represent certified samples, the calibration curve is calculated based on the principle: the sum of the squares of the deviation  $\sum \Delta^2 = \min$ . From the best fit, curve should become minimum. Assuming that the given analyses are accurate to any required degree, the SR is calculated:

$$SR = \pm \frac{\sum \Delta^2}{n - a}$$

Where  $a = 2$  for a straight line,  $a = 3$  for a parabola,  $a = 4$  for a cubic curve.

If numerous samples have been used for calibration, the SR can also be determined in graph form as follows: the envelope curve is drawn round all points in the coordinate system. The distance is equivalent to  $4\text{ SR}$  ( $= \pm 2\text{ SR}$ ) which includes 96% of all values. In  $\pm 1\text{ SR}$ , 67% of all values are to be found (See the figure below). The standard error SR is a measurement of analytical accuracy.

## Applications

### 1) Steel Industry

The ferrous industry produces a wide range of different products, such as cast iron; low and high steel alloys, stainless and tool steel products. For process control, the fast analysis of the iron and steel is important. The accurate analysis of nickel with high precision will allow realizing savings by adjusting the nickel level to the possible lowest level. However, the process benefits are as well from the analysis of raw materials (ores, coal, limestone) and important process materials (slags, ferro alloys, refractories and sinters). In non-ferrous industry, different elements are monitored in the process to ensure that the specified composition of the Lead-, Cobalt-, Nickel- or Copper based alloy is met. The shortest time to analysis and high analytical speed is also required for the production of precious metal alloys and high purity copper. Optical Emission Spectrometers are worldwide used for the element analysis in all fields of the metal production and metal processing industry.

Foundries and steel plants well as roller mills, automotive supplier and metal traders. There the element analysis is essential for process and quality control. With Optical Emission Spectrometers, all relevant elements can directly be analyzed simultaneously from very minute concentrations to percentage levels. Thanks to the method precision and the short analysis time, this equipment represents a valid control system of production in all the fields regarding metal industry (primary alloys foundries, metal processing industries, mechanical industry) in any time during production cycle, in the case it is necessary to have a fast and accurate chemical analysis of material.

## 2) *Surgical Industry*

Stainless steel is used extensively in the biomedical industry including catheters, stents, screws, tubing, guide wires, dental products, orthopedics and wide variety of medical instruments. Stainless steel is often the metal of choice i.e. preferable alloy for surgical parts because of its resistance to corrosion.

## 3) *Auto Industry*

As the automotive industry addresses environmental concerns, the problem of fuel consumption and weight reduction has come to the fore. Reducing the weight of automobiles is one of the primary means by which their fuel consumption is lowered. The two basic approaches are in automotive design and in materials selection which are closely related. Regarding materials, there has been a trend toward the use of light metals and metallic alloys in automotive components, particularly automotive bodies. The most commonly used materials are aluminum, magnesium, and their alloys, though some research has also been done on the use of titanium, zinc, and nonmetallic materials.

The analysis of aluminum and its alloys is the second most prominent analytical application for today's spark spectrometers. Besides the traditional commercial applications for this metal, the automotive industry has recently led to rapid alloy developments. These alloys have become popular in automotive manufacturing thanks to its light weight and improved properties.

## Conclusion

The remarkable advances have been reviewed made in the use of optical emission spectrometers over the last 20 years and especially in the combination of allied technologies such as computers, fibre optics, holographic gratings and high speed electronics, and it is indeed to appreciate the considerable contribution to man's quest to improve materials through excellent analyses.

Only through better materials and a better understanding of the processes required to produce them, will man's restless quest for a better way of life be realized.

## REFERENCES

- <http://www.azom.com/materials-equipment.aspx?cat=35>
- [http://www.ehow.com/list\\_6111657\\_uses-optical-emissions-spectrometer.html](http://www.ehow.com/list_6111657_uses-optical-emissions-spectrometer.html)
- <http://nvl.nist.gov/pub/nistpubs/jres/100/4/j14rob.pdf>
- [http://www.bruker-axs.com/aluminium\\_metallurgy.html?L=4](http://www.bruker-axs.com/aluminium_metallurgy.html?L=4)
- <http://www.iupac.org/publications/pac/pdf/1993/pdf/6512x2443.pdf>
- Metal-Lab 75/80V,GNR.S.r.l,info@gnr.it
- novelresearchinstitute.org/library/SpectroscopyOvrview.pdf
- Pure & App. Chem. Vol.65, No.12, pp.2243-2452, 1993.
- www.eaglabs.com/files/appnotes/BN1500.pdf
- www.gnr.it/pages/OES.php?Pg=all

# Effect of Composition on Structure and Mechanical Properties of Metakaolin Based PSS-Geopolymer

Najet Saidi<sup>1</sup>, Basma Samet<sup>\*2</sup>, Samir Baklouti<sup>3</sup>

Laboratoire de Chimie Industrielle, Ecole Nationale d'Ingénieurs de Sfax, BP W 3038, Sfax, Tunisia

<sup>1</sup>essaidi.najet@hotmail.fr; <sup>\*2</sup>sametbasma@yahoo.fr; <sup>3</sup>baklouti.samir@gmail.com

## Abstract

Geopolymer is a type of cross linked long-chain inorganic compound, built in three-dimensional structures and has different attractive properties (thermal, mechanical, chemical, etc).

This study elucidated the structure and mechanical properties of PSS type geopolymer obtained by alkaline attack of metakaolin. A systematic investigation was conducted to comprehend the effect of molar ratios Si/Al and Na/Al on the properties of this geopolymer by using <sup>29</sup>Si and <sup>27</sup>Al magnetic angle spinning nuclear magnetic resonance (MAS NMR) spectroscopy, X-Ray diffraction and mechanical measurements. The results indicate that an increase of Si/Al ratio improves the geopolymer mechanical properties due probably to the formation of Si-O-Si bond in the geopolymer at the expense of Si-O-Al one. It was also shown that an introduction of NaOH in the geopolymer composition enhances the mechanical properties until a molar ratio Na/Al=1. Beyond this value, the excess of Na<sup>+</sup> cation causes fragility of the geopolymer structure confirmed by a decrease of the mechanical strength.

## Keywords:

Geopolymer; Metakaolin; Structure Evolution; <sup>29</sup>Si; <sup>27</sup>Al NMR; XRD Resolution; Alkali Activation

## Introduction

"Geopolymers", ill-organized polymeric aluminosilicate materials obtained by alkaline or alkaline-earth activation of aluminosilicates, were introduced into the inorganic cementious by Davidovits in 1970 (Komnitsas & Zaharaki 2007). According to the molecular structure; geopolymeric binder can be expressed by the following empirical formula  $M^{+n} \{(\text{SiO}_2)_z, (\text{AlO}_2)_n, w \text{H}_2\text{O}\}$  where M is a cation such as potassium (K) or sodium (Na); n the degree of polycondensation; z is 1, 2 or 3, then geopolymer is termed as PS; PSS or PSDS respectively; w is binding water amount. These structures consist of a polymeric Si-O-Al framework, similar to that found in zeolites.

The main difference with zeolitic structures is that geopolymers are amorphous to X-rays diffraction.

Geopolymers are currently of large interest, due to their good thermal, chemical and mechanical properties and their potential as "green" cementitious binder (Duxson, Fernandez-Jimenez, Provis, Lukey, Palomo & Van Deventer). Geopolymerization involves an exothermic reaction between an alumino-silicate pre-cursor, such as metakaolin for instance, and a high alkalinity silicate solution (Davidovits 1994). Xu and Van Deventer (2002) considered that the basic steps of geopolymerization are the dissolution of the solid alumino-silicate oxide in the MOH solution (M: alkali metal), the diffusion of dissolved Al and Si complexes from the particle surface to the inter-particle space, the formation of a gel phase resulting from the polymerization between the silicate solution and Al and Si complexes, and finally, the hardening of the gel phase.

Many materials composed of silica and alumina can be used in order to synthesize geopolymers. Indeed, many investigations have used metakaolin, Kaolinitic clays, fly ashes sand blast furnace slags as raw materials (Pacheco-Torgal, Castro-Gomesb, & Jalali 2008). It was demonstrated that the reactivity of these materials is higher when its amorphous content is higher.

The most used alkaline activators are mixture of sodium or potassium hydroxide with sodium or potassium waterglass.

In addition to water content, Divya and Rubina (2007) reported that parameters of geochemistry reaction for geopolymer system include the molar ratios  $M_2\text{O}/\text{SiO}_2$  and Si/Al and the concentration of MOH (where M is Na or K element).

The objective of this paper was to study the effect of Si/Al and Na/Al ratios on a PSS metakaolin based

geopolymer structure. XRD, MAS-NMR and DTA, TGA techniques have been applied to analyze the structure of the synthesized geopolymers. The correlation between mechanical strength and geopolymer structure has also been considered.

## Materials and Experimental Techniques

### Materials

Different raw materials are used in this work:

- Metakaolin: used as aluminosilicate raw material and obtained by calcining kaolin (supplied by CHEMI-PHARMA Company) at 700 °C for 5 h.
- Analytical reagents NaOH pelled (purity = 99.5%) and sodium silicate solution (Si/Na=1.5,  $\rho=1.39\text{g}/\text{cm}^3$ ) used as alkaline reagents.
- Distilled water

### Geopolymer Synthesis

Geopolymer samples were prepared by:

- mixing sodium silicate and NaOH pellets together 24h before use ;
- adding metakaolin to the alkaline solution and mixing until the paste is homogenous ;
- All the mixtures are prepared with a constant Solide/Liquide ratio equal to 1.8.
- after mixing, paste specimens were poured in 32 mm diameter plastic containers and then cured at ambient temperature for 7 days.

### Experimental Techniques

The raw material and geopolymers mineral phases are identified by X-ray diffraction (XRD) using a « BRUKER-AXS-D8-Advance. The XRD patterns are obtained with a scanning rate of  $1^\circ\text{min}^{-1}$  from  $5^\circ$  to  $60^\circ$  (2 $\theta$ ). The wavelength is selected as 15.40562nm (Cu). Phase identification is made using files JCPDS (Joint Committee Powder Diffraction Standard).

The characterisation of these materials is also performed by:

- Simultaneous DTA and TGA measurements using(Set Soft 2000). Experiments are carried out between 25°C and 1200°C at a heating and cooling rates of 10°C/min with a helium gas purge.
- $^{27}\text{Al}$  and  $^{29}\text{Si}$  MAS NMR using a Bruker ASX500 (7T magnetic field) spectrometer, operating at 15 KHz for  $^{27}\text{Al}$  and 8 KHz for  $^{29}\text{Si}$ .
- Brazilian test on geopolymer samples (6mm height and 32 mm diameter) in order to assess the

mechanical properties. At least six samples of each formula were tested. The average value is served as the ultimate compressive strength. The loading is displacement controlled at a constant rate of  $0.5\text{mm min}^{-1}$  for all the compression tests. All samples were tested after 7 days of curing.

## Results and Discussions

### Characterization of Kaolin

The chemical composition of kaolin (Table 1) shows that, in addition to silica and alumina, the sample contains  $\text{Fe}_2\text{O}_3$ , CaO,  $\text{K}_2\text{O}$  and MgO.

TABLE 1 CHEMICAL COMPOSITION (MASS %) OF KAOLIN

SiO <sub>2</sub>	Al <sub>2</sub> O <sub>3</sub>	Fe <sub>2</sub> O <sub>3</sub>	MgO	Na <sub>2</sub> O	CaO	K <sub>2</sub> O	LOI
44.7	36.55	1.69	0.27	1.83	1.81	0.73	12

XRD analysis (Fig. 1) of the kaolin before and after calcination shows that the used clay contains, in addition to kaolinite, some illite and quartz. The calcination of kaolin, transforms kaolinite to an amorphous material confirmed by the presence of a halo between  $20^\circ$  and  $30^\circ$  (2 $\theta$ ), while quartz and illite remain unchanged.

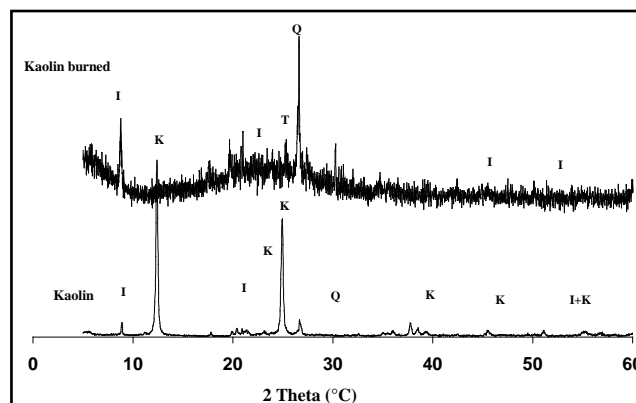


FIG. 1 X-RAY DIFFRACTION PATTERNS OF KAOLIN BEFORE AND AFTER CALCINATION

K: Kaolinite, Q: quartz, I: illite, T: TiO<sub>2</sub>

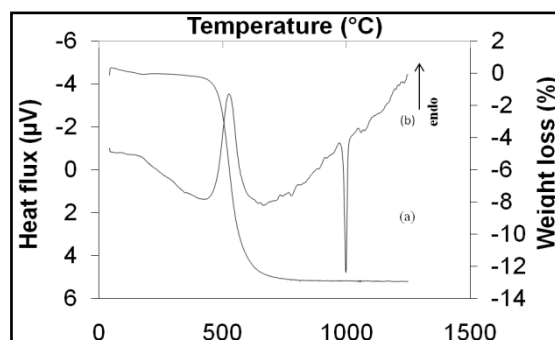


FIG. 2 DTA-TG THERMOGRAMS OF KAOLIN:

(a) ATG, (b) ATD

The DTA/TG curves of this kaolin are presented in Fig. 2. The main changes pointed out during the heating

are the following:

- $T < 100^\circ\text{C}$ : endothermic release of the free water,
- $430\text{--}620^\circ\text{C}$ : endothermic dehydroxylation of kaolinite and formation of metakaolinite,
- $\sim 970^\circ\text{C}$ : exothermic reorganization of the metakaolinite structure (recrystallization).

Was minded that the amorphous state is obtained when the clay is heated at a temperature between the end of dehydroxylation and the beginning of recrystallization. Consequently the chosen calcination temperature for the present study is  $700^\circ\text{C}$ .

### Effect of Si/Al Ratio

In order to understand the effect of Si/Al molar ratio on the structures and mechanical properties of geopolymer, different mixtures were prepared with Si/Al molar ratios varying from 1.8 to 2.33 as shown in Table 2, by introducing different amounts of sodium silicate.

TABLE 2 COMPOSITIONS AND MECHANICAL STRENGTHS OF GEOPOLYMER SAMPLES PREPARED AT DIFFERENT MOLAR SI/AL RATIOS (AMOUNT OF NaOH = 0.35g)

Geopolymer	Si/Al (molar ratio)	Na/Al (molar ratio)	Compressive Strength (MPa)
Geop a	1.80	0.531	2.1
Geop b	1.96	0.638	3.6
Geop c	2.19	0.793	4.9
Geop d	2.33	0.886	5.5

This domain is selected in order to obtain PSS geopolymer type. The used amount of NaOH introduced is constant in all mixtures (amount of NaOH = 0.35 g).

It is interesting to notice that the adjunction of sodium silicate in order to increase Si/Al ratio induces inevitably an increase of Na/Al ratio too.

The results of mechanical characterization of the obtained samples are presented in Table 2 and Fig. 3.

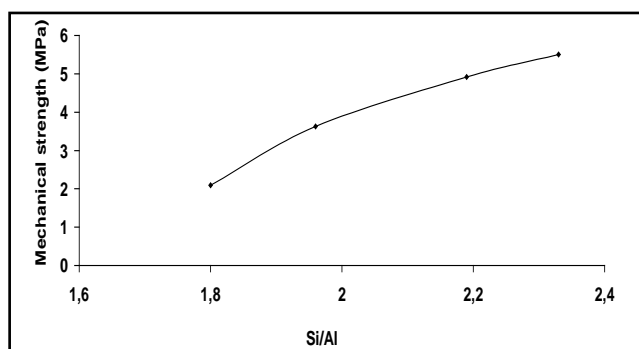


FIG. 3. COMPRESSIVE STRENGTH EVOLUTION OF GEOPOLYMER WITH Si/Al MOLAR RATIOS

It was noticed that the geopolymer compressive

strength increases with increasing Si/Al ratio. In fact, the mechanical strength value of geopolymer with Si/Al = 2.33 is almost three times that of geopolymer with Si/Al = 1.8. This behavior can be mainly attributed to the formation of stronger Si-O-Si bonds at the expense of Si-O-Al ones (Duxson, Provis & Lukey 2005). It is interesting to note that the increase of the mechanical properties is not only related to Si/Al ratio but also to that of Na/Al.

### 1) X-ray Diffraction Analyses

In order to elucidate in a microscopic scale the evolution of the compressive strength for different synthesized geopolymers, XRD technique was employed to characterize the structure of these geopolymers.

The results of X-ray diffraction analysis of metakaolin and geopolymer synthesized at different Si/Al ratios are shown in Fig. 4 revealing a halo diffraction pattern from almost  $15^\circ$  to  $35^\circ$  ( $2\theta$ ) for all geopolymers, showing that these materials are amorphous. (Derrien 2004).

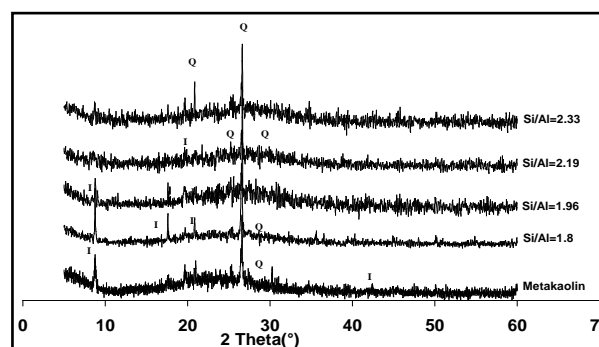


FIG. 4 DIFFRACTOGRAMS OF METAKAOLIN AND GEOPOLYMERS SYNTHESIZED AT Si/Al RATIOS  
Q: quartz; I: illite

Some peaks related to crystallized phases were also detected, which is attributed to quartz and illite initially present in the kaolin and which has not contributed to the polymerization.

In addition, it was noted that the intensity of the peaks relative to illite decreases when the Si/Al ratio increases (Na/Al increases also). This evolution indicates that with high amount of sodium silicate, illite is probably dissolved and contributes to the geopolymerisation.

The diffractogram of the geopolymer with Si/Al=1.8 shows some peaks which are not present in the others geopolymer spectra indicating more orderly phases in this material. This is probably due to the local formation of crystalline phase zeolit which is consistent with the results of Duxson, Fernandez-



water caused by the condensation of silanol or aluminol groups (dehydroxylation) on the surface of geopolymer.

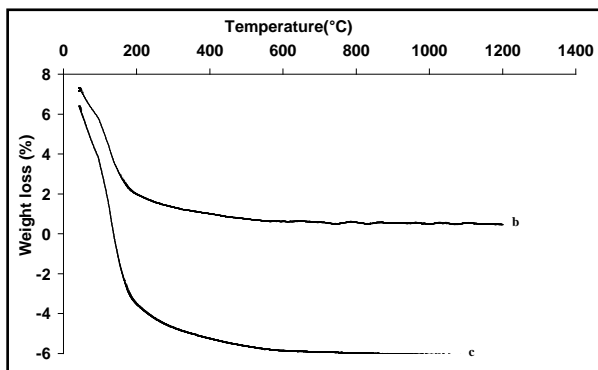


FIG. 8 TG THERMOGRAMS OF Na-GEOPOLYMERS OBTAINED AT DIFFERENT Si/Al RATIOS: b:Si/Al=1.96, c:Si/Al=2.19

Moreover, the DTA thermogram (Fig. 7) corresponding to the geopolymer with Si/Al=1.8 (Geop a) shows exothermic peaks around 966°C and 1070°C, without any mass change in the TGA thermogram (Fig. 8). It can be attributed either to the transformation of residual metakaolinite into mullite phase and/or to the destruction of zeolite structure formed in the geopolymer with Si/Al =1.8, which was proved by XRD.

**Effect of NaOH**

In order to study the effect of the alkaline solution (NaOH ) amount on the properties of geopolymer, we have prepared the same geopolymers but in the presence of 0.7 g NaOH. The composition and the properties of these geopolymers are shown in Table 4.

TABLE 4 COMPOSITIONS AND COMPRESSIVE STRENGTHS OF GEOPOLYMER SAMPLES PREPARED WITH 0.7g NaOH

Geopolymer	Si/Al	Na/Al	Compressive strength (MPa)
Geop a'	1.8	0.859	2.8
Geop b'	1.96	0.965	4.0
Geop c'	2.19	1.12	3.6
Geop d'	2.33	1.214	2.8

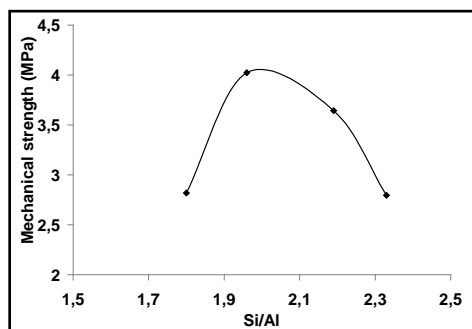


FIG. 9 COMPRESSIVE STRENGTH EVOLUTION OF GEOPOLYMERS PREPARED WITH DIFFERENT Si/Al MOLAR RATIOS (USING 0.7g OF NaOH)

According to the results presented in Fig. 9, the compressive strength of geopolymer samples increases with Si/Al ratio to reach maximum when Si/Al=1.96 corresponding to Na/Al=0.965≈1. This behaviour is the same as that observed previously and explained by the formation of Si-O-Si bonds at the expense of Si-O-Al ones. For higher Si/Al ratio, the compressive strength decreases due probably to the structure fragilisation of geopolymer by the excess of Na<sup>+</sup> cation in the mixture comparatively to the amount of Al<sup>3+</sup>.

It is well known that the Na<sup>+</sup> cations are needed in geopolymerisation to compensate the negative charge imbalance created when Al forms tetrahedra in geopolymer structure. This means that the number of needed Na<sup>+</sup> cations must be equal to that of the transformed Al tetrahedra (Na/Al=1) in the geopolymer.

Fig. 10 shows the variation of geopolymer compressive strength with Si/Al molar ratio at different amounts of NaOH. It is clear that until Si/Al≈2, compressive strength increases with Si/Al ratio independently of the NaOH amount.

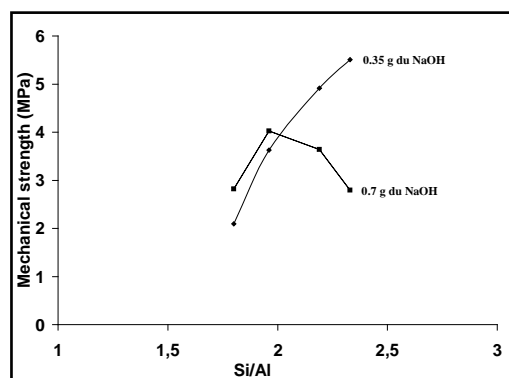


FIG. 10 EVOLUTION OF COMPRESSIVE STRENGTH WITH Si/Al RATIOS AT DIFFERENT AMOUNTS OF NaOH

For higher Si/Al ratio, if Na/Al molar ratio is lower than 1 (case of geopolymers with 0.35 gNaOH), compressive strength continues to increase, if not compressive strength decreases (case of geopolymer with 0.7 g NaOH) then the amount of alkaline solution must be well calculated before preparing geopolymer.

TABLE 5 <sup>29</sup>Si AND <sup>27</sup>Al NMR ANALYSES OF GEOPOLYMERS WITH Si/Al=2.33

Na/Al	0.886 (0.35g NaOH)	1.214 (0.7g NaOH)
Compressive strength(MPa)	5.5	2.8
Si δ (ppm)	-92.16	-89
Al δ(ppm)	55.4	56.38

In order to explain the difference between the compressive strengths measured on geopolymers containing different amounts of NaOH, <sup>29</sup>Si NMR analyses were performed on samples with Si/Al ratio

equal to 2.33 containing 0.35 and 0.7 g NaOH. The obtained results are presented in Table 5.

It was noticed that the increase of Na/Al to a value higher than 1, induces a decrease of the mechanical strength and a shift of  $^{29}\text{Si}$  NMR signal to lower values, which is probably a sign of structure fragility and that  $^{27}\text{Al}$  NMR signal is not very sensitive to the Na/Al ration variation.

Although the increase in the amount of NaOH has promoted geopolymerization reaction, it hasn't a significant influence on X-ray diffractograms of geopolymers (Fig. 11).

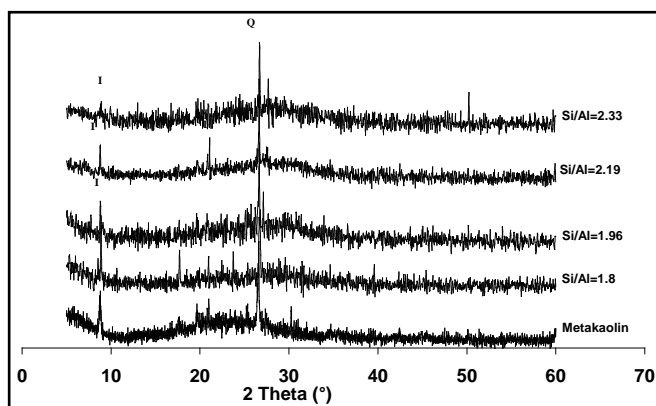


FIG. 11 DIFFRACTOGRAMS OF METAKAOLIN AND GEOPOLYMERS SYNTHESIZED AT DIFFERENT Si/Al RATIOS WITH 0.7g NaOH

Indeed, it was noticed that when the Si/Al increases, the position of the diffuse halo moves to the highest angles whatever the amount of NaOH, but the phenomenon is more marked in the presence of 0.7g of NaOH (Fig. 12).

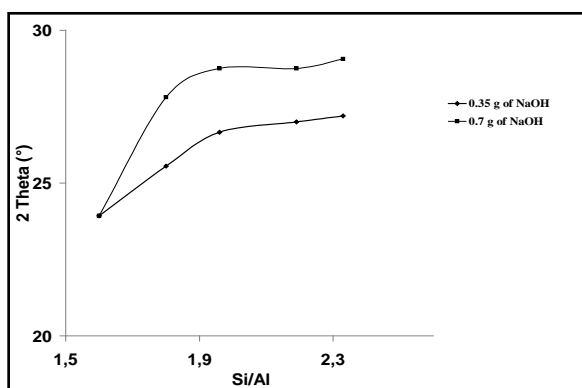


FIG.12. VARIATION OF THE CENTER POSITION OF THE HALO FOR GEOPOLYMERS HAVING DIFFERENT Si/Al RATIOS AT DIFFERENT AMONTS OF NaOH

## Conclusion

The objective of this work has focused primarily on the synthesis of Polysiloxosialate geopolymer (PSS) from kaolin calcined at 700°C for 5 h, and to study the effect

of a number of experimental parameters on the properties of geopolymer.

The increase of Si/Al ratio induces:

- the improvement of the geopolymer mechanical strengths,
- the formation of amorphous geopolymers regardless of the Si/Al ratios except for Si/Al=1.8, we have seen the formation of local zeolitic crystallized structure,
- the increase of weight loss (detected by thermogravimetric analysis) between ambient temperature and 200°C attributed to the elimination of free pore water, and between 200 and 600°C related to condensation of silanol and aluminol groups
- the shift of the broad peak in  $^{29}\text{Si}$  NMR spectra from -92 ppm for Si/Al = 2.33 to -86ppm for Si/Al = 1.8,
- the contribution of illite to the geopolymerisation.

Increasing the amount of NaOH during geopolymer synthesis leads to:

- an overall increase in mechanical strength due to an easier dissolution step, but beyond a Si/Al =1.96 mechanical strength decreases due to the fragility of the structure of geopolymer by the excess of Na<sup>+</sup> cation comparatively to Al<sup>3+</sup>.
- the existence of an amorphous state for the prepared geopolymers (detected by XRD) and a shift of the angle 2θ corresponding to the center of the halo indicating the geopolymerization evolution.

## REFERENCES

- Davidovits, Joseph. "Geopolymers: Inorganic polymeric new materials" *Journal of Materials Education* 16 (1994): 91-138.
- Derrien, Anne-Cécile. "Synthèse et caractérisation physico-chimique de géopolymères. Application : Cinétique de minéralisation de géopolymères et du biomatériau CaCO<sub>3</sub> synthétique" Thèse de doctorat, Université de RENNES 1, 2004.
- Divya, Khale. and Rubina, Chaudhary. "Mechanism of geopolymerisation and factors influencing its development: a review" *Journal of Material Science* 42 (2007): 729-746.
- Duxson, Peter., Provis John L. and Lukey Grant C., "Understanding the relationship between geopolymer

- composition, microstructure and mechanical properties" *Colloids and Surfaces. A: Physicochemical Engineering Aspects* 269 (2005): 47-58.
- Duxson, Peter., Fernandez-Jimenez, A., Provis, John L., Lukey, Grant C., Palomo, Angel. and Van Deventer Jannie S.J. "Geopolymer technology: the current state of the art" *Journal of Material Science* 42 (2007): 2917-2933.
- Komnitsas, Konstantinos. and Zaharaki Dimitra. "Geopolymerisation: A review and prospects for the mineral industry" *Minerals Engineering*. 20 (2007).1261-1277
- Pacheco-Torgal, Fernando., Castro-Gomesb, João. and Jalali, Said. "Alkali-activated binders: A review. Part 2. About materials and binders manufacture" *Construction and Building Materials*, 22 (2008): 1315-1322.
- Xu Hong., Van Deventer Jannie S.J. "Microstructural characterisation of geopolymers synthesized from kaolinite/stilbite mixtures using XRD, MAS-NMR, SEM/EDX, TEM/EDX and HREM" *Cement and Concrete Research* 32 (2002): 1705-1717.
- Yao, Xiao, Zhang, Zuhua., Zhua, Huajun. and Chen, Yue. "Geopolymerization process of alkali-metakaolinite characterized by isothermal calorimetry" *Thermochimica Acta* 493 (2009): 49-54.
- Zibouche, Fatima., Kerdjoudj, Hacène. and Van Damme, Henri. "Geopolymers from Algerian metakaolin. Influence of secondary minerals" *Applied Clay Science* 43 (2009): 453-458.
- Zuhua, Zhang, Xiao Yao, Huajun, Zhu. and Yue C., "Role of water in the synthesis of calcined kaolin-based geopolymer" *Applied Clay Science* 43 (2009): 218-223.

# Compatibility in Immiscible Poly(Vinyl Chloride)/Poly(Styrene) Blends

V. D. Deshpande<sup>\*1</sup>, Pravin Pawar<sup>2</sup>, Vinod Gokarna<sup>3</sup>

<sup>1,2,3</sup>Department of Physics, Institute of Chemical Technology, India

<sup>\*1</sup>vindesh2@rediffmail.com; <sup>2</sup>pravinpawar@gmail.com; <sup>3</sup>py07vs.gokarna@pg.ictmumbai.edu.in

## Abstract

The morphology, orientation and mechanical studies of solvent cast poly (vinyl chloride) (PVC) /poly (styrene) (PS) blend films were carried out for various concentrations and draw ratios. Samples of pure PVC, PS and its blends were prepared using standard solution casting method.

The thermal studies revealed that PVC/PS blends remain 'incompatible' for the compositions PVC/PS-80/20, 60/40, and 30/70; compatibility is suggested for the compositions PVC/PS-20/80, 10/90 and 05/95. Microscopy results indicate that PVC/PS 20/80, 10/90 and 05/95 blends show uniform distribution of PVC dispersed phase in PS matrix phase. Orientation studies showed that PVC/PS-20/80, 10/90 and 05/95 blend compositions gave a systematic change in orientation function with draw ratio; matching with their respective pure forms; while all other blend compositions indicate independent random orientation behaviour. The mechanical properties like storage modulus and tensile strength of the blends PVC/PS-20/80, 10/90 and 05/95 are very close to pure PVC. The blends 80/20, 60/40, and 30/70 showed inferior properties to pure PVC for all draw ratios. The results were explained in terms of morphology of the blends.

## Keywords

PVC; Immiscible; FTIR; PS

## Introduction

Molecular orientation of uniaxially stretched polymer blends has been the subject of several studies. The orientation of polymer chains, one of the important factors affecting the mechanical properties of polymers, in a blend is an attractive study because in a blend two components may possibly orient in different ways leading to the formation of a new superstructure. Several techniques exist for evaluation of such behaviour e.g. X-ray Diffraction, Birefringence, Sonic Modulus, Polarized Raman Spectroscopy and Infrared Spectroscopy. Most of the studies of the orientation behaviour have been carried out on 'compatible' blends. Chabot and Prudhomme studied the segmental orientation in PVC and poly ( $\alpha$ -methyl- $\alpha$ -n-propyl- $\beta$ -propiolactone) (PMMPL). Deshpande and Singh have

shown the effect of miscibility on orientation in PVC and poly (methyl methacrylate) (PMMA) blends. The segmental orientation in PVC with polycaprolactone (PCL) and nitrocellulose (NC) were studied by Hubbell and Cooper. Keroacka, et al studied the effect of molecular orientation in crystalline and amorphous phases for PVC/PCL blends. These polymers were fully or partially miscible with PVC. There have been very few studies on the orientation behaviour of immiscible polymer blends. In most of the cases, it is observed that the major component orients to higher degree than the minor dispersed component, which is again dependent on the stretching temperature. The resultant morphology has a significant effect on the overall deformation behaviour.

The blend of interest in this study is PVC /poly (styrene) PS; and PVC/PS blends are reported immiscible due to unfavourable interactions. This would affect the morphology by means of controlling the domain size.

In the present studies, PVC/PS blends have been prepared with different compositions in the film form using solution casting method. The objective of the present work was to investigate the influence of morphology of blends on the orientation and mechanical properties of the blends and to gain further understanding of the orientation behaviour in the multiphase incompatible polymer blends.

## Experimental

### Materials

The analytical grade polymers, PVC with  $M_w$  of 94,000 and  $\rho=1.40$  g/cm<sup>3</sup>; PS with  $M_w$  of 100,000 and  $\rho=1.05$  g/cm<sup>3</sup> obtained from Aldrich Chemical Co. were used in this study.

The samples of pure PVC, PS and PVC-PS blends were prepared using standard solution casting method. First of all, the two polymers were mixed in proportions as PVC/PS-100/00, 80/20, 60/40, 30/70, 20/80, 10/90, 05/95 and 00/100. Keeping the total

weight of the polymers as 3% w/v; they were dissolved in constant amount of common solvent Tetrahydrofuran (THF), (Spectroscopic grade, S.D. Fine Chemicals). Films were prepared by casting the solutions of polymers on a clean and flat glass plate (Petri-dish) in the oven at 50°C for 3 h; then further annealed at 60°C till the disappearance of 1065 cm<sup>-1</sup> THF absorption band which ensures complete removal of solvent THF from films. The films of pure and blend polymer samples thus prepared were around 40 μm in thickness.

### Preparation of Stretched Samples

Sample films were cut in 4 x1 cm<sup>2</sup> strips. Each strip was clamped vertically at its extreme ends between the two jaws of Universal Tensile Machine (UTM). The gauge length between the two jaws was set at 2 cm. The strip was then heated to 120°C in a closed chamber attached to UTM. The temperature of 120°C was chosen as it is well above the glass transition temperatures of both PVC (82°C) and PS (98°C) and samples showed maximum orientation at this temperature. A minimum of 10 minutes was allowed for the sample to attain the desired temperature. The strip was then stretched with constant strain rate 0.008s<sup>-1</sup>. The draw ratio taken was the ratio of the final stretched length (l) to the initial length (l<sub>0</sub>) of the sample. The procedure was done for different draw ratios i.e. for draw ratios (λ) 1.25, 1.5, 1.75, 2, 2.25, 2.75, and 3. The sample was immediately quenched in ice after the completion of stretching, to lock the orientation.

### Thermal Studies

The glass transition temperature (T<sub>g</sub>) of pure polymers and their blends were found out using Perkin-Elmer Differential Scanning Calorimeter (DSC-7). The instrument was calibrated with an Indium standard and the measurements were conducted under continuous nitrogen flow. The weight of the sample used in DSC pan was kept constant as 10 mg and heating rate was set at 20°C/min.

Dynamic mechanical thermal analysis (DMTA) was carried out with direct reading Eplexor R, Gabo Ltd. at 5 Hz as an oscillatory frequency. The storage (E') and loss (tan δ) moduli were measured over the temperature range 40-120°C at a heating rate of 5°C/min under nitrogen stream. All measurements were done on unoriented solution cast films.

### FTIR Studies/Infrared Dichroism Studies

FTIR spectra of unstretched samples were recorded in

the range 4000 to 400 cm<sup>-1</sup> at resolution 2 cm<sup>-1</sup> using Perkin-Elmer-Spectrum 100 FTIR Spectrophotometer. For orientation studies, the polarization of the incident beam was achieved by the use of Perkin-Elmer gold wire grid polarizer. The samples rather than the polarizer were rotated through 90° in order to obtain the parallel and perpendicular polarization measurements. In this way, spectra were recorded for all stretched samples to find out absorbance in parallel and perpendicular direction.

### Orientation Function Measurements by Infrared Dichroism

Infrared dichroism occurs because absorption by a particular functional group occurs only at a specific angle with stretching direction which is represented by a transition moment vector. If a polymer is elongated such that these vectors are preferentially oriented, the amount of absorbance of plane-polarized light parallel to the direction of stretch (A<sub>||</sub>) will differ from the absorbance of plane-polarized light perpendicular to the direction of stretch (A<sub>⊥</sub>). The ratio of these two absorbances is called the dichroic ratio D,

$$D = A_{||}/A_{\perp}$$

This varies from zero to infinity, with unity representing random orientation. The orientation function f<sub>M</sub> of transition moment vector can be related to the stretch direction by the following expression,

$$f_M = \left( \frac{D-1}{D+2} \right)$$

To relate the orientation of the polymer chain to the stretch direction, one must assume that all orientations of f<sub>M</sub> about the chain axis are equally probable. The resulting transformation gives,

$$f_M = \left( \frac{D_0+2}{D_0-1} \right) \left( \frac{D-1}{D+2} \right) \quad (1)$$

where D<sub>0</sub> is the dichroic ratio for perfect orientation and is related to the angle α between the transition moment vector and the chain axis by the following equation:

$$D_0 = 2 \cot^2 \alpha$$

Thus, with the knowledge of the angle α and the measurement of A<sub>||</sub> and A<sub>⊥</sub>, one can calculate the orientation function of the polymer chain.

### Morphology Studies

The solution cast film samples for optical examination were prepared by sandwiching the films between glass slides and cover slips. Olympus BX51 microscope attached with a camera system Olympus DP 12 was used for studying the phase dispersion

morphology of minor components in matrix component for these blends.

Further, samples were also subjected to scanning electron microscopy (SEM). The films were examined in an instrument model JSA JEOL 6380 LA analytical SEM with 20KV accelerating voltage and SPI sputter coater (Model JEOL -JFC-1600). Auto fine coater was used to coat the surfaces with gold to enhance conductivity.

**Mechanical Studies:**

The mechanical studies were carried out using Universal Tensile Machine (UTM) (LLYOD Instruments-LR-10K PLUS). The measurements of the mechanical properties of the stretched samples were done at room temperature.

**Results and Discussion**

**Thermal Studies**

The previous studies reported on the miscibility behaviour of PVC/PS blends have reported different conclusions, ranging from complete immiscible when melt blended to miscible when cast from the common solvent.

In the present case, the 'compatibility' of the PVC/PS blends is characterized by employing DSC and DMTA techniques. Throughout 'compatibility' was considered as molecular dispersion of one component into the other; hence 'compatibility' need not be miscibility. The first indication of blend 'compatibility' is a single composition dependent Tg. The Fox equation is

$$\frac{1}{T_g} = \frac{W_1}{T_{g1}} + \frac{W_2}{T_{g2}} \tag{2}$$

and Wood equation is

$$T_g = W_1 T_{g1} + W_2 T_{g2} \tag{3}$$

where Tg is the expected glass transition temperature of the miscible blend, Tg1 and Tg2 are those of pure PVC and PS respectively, and W1 and W2 are the corresponding weight fractions. Fig. 3 shows Tg's obtained from DMTA and calculated using Fox equation and wood equation.

Tg's, obtained from DSC of pure PVC and Pure PS is 82°C & 98°C respectively. As shown in Fig. 1, two glass transition temperatures were obtained for the blend compositions PVC/PS- 80/20, 60/40 and 30/70. The two Tg's obtained corresponding to their homopolymer glass transitions are due to each component gaining segmental mobility independent of the other as a result of their 'incompatibility' at different

temperatures. Single Tgs' was obtained for the blends with compositions PVC/PS-20/80, 10/90 and 05/95 which indicate 'compatibility' of these blends for said compositions. As PVC and PS have Tg values which are quite close, it was thought worthwhile to use highly sensitive DMTA technique to further investigate the 'compatibility'.

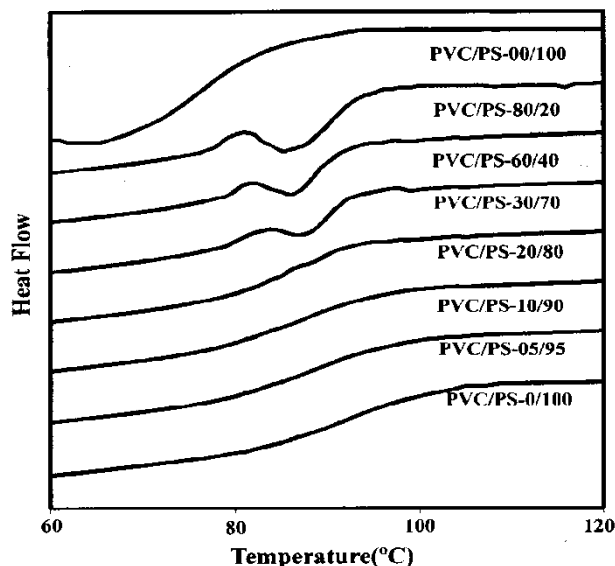


FIG. 1 DSC CURVES OBTAINED FOR PURE PVC, PS AND THEIR BLENDS

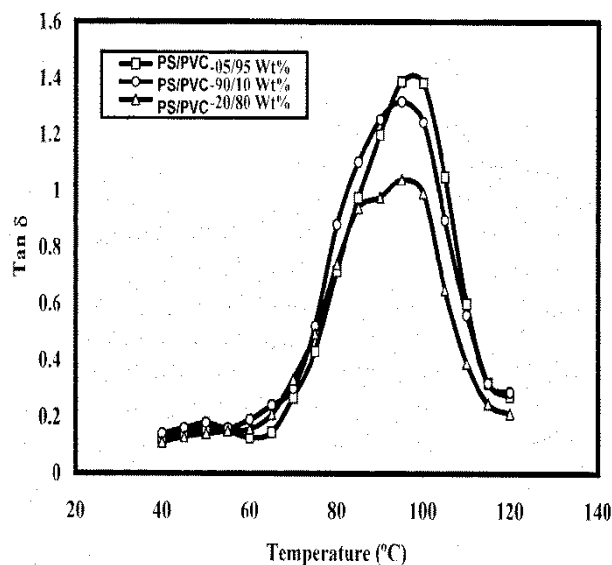


FIG. 2 DMTA CURVES OBTAINED FOR PS/PVC BLENDS

The results obtained from DMTA are shown in Fig. 2 for the compositions PVC/PS-20/80, 10/90 and 05/95. The curves in Fig. 2 show damping (tan delta) versus temperature data for PVC/PS blends. The maxima of tan delta is observed at a temperature where the loss in energy during cyclic stress on the sample occurs due to additional degree of freedom, which is a measure of Tg associated with alpha-relaxation of the polymeric material. The pure PVC shows a Tg at 80°C whereas

the pure PS shows it at 98°C. The PVC/PS 20/80 blend shows two relaxation transition peaks which correspond to the T<sub>g</sub> values of pure PVC and PS, respectively, indicating separate presence of pure PVC and PS phase in the blend. This indicates that PVC/PS 20/80 blend is showing immiscibility. The other blend compositions PVC/PS-10/90 and 05/95 show single relaxation transition peak.

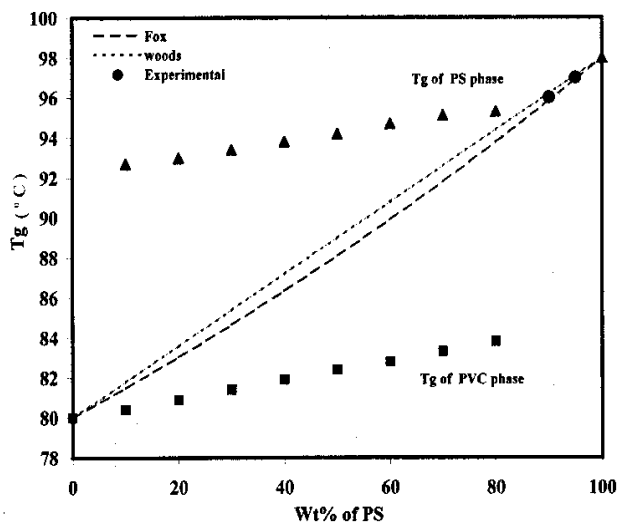


FIG. 3 COMPARISON OF OBTAINED TG FROM DMTA WITH FOX AND WOOD EQUATION

It is apparent from Fig.(3) that the experimental T<sub>g</sub>'s of two blend compositions PVC/PS- 10/90 and 05/95 are nearly same as the T<sub>g</sub>'s obtained from equation (2) and (3). The single T<sub>g</sub> in a polymer-polymer blend can be due to either molecular level mixing of individual polymers or two separate phases distributed uniformly at micro-level. Hence the blend compositions PVC/PS- 10/90 and 05/95 can have either of the two and be considered 'compatible' as per thermal study.

Thus it is concluded that the present PVC/PS blend samples prepared by the above described experimental conditions and particularly with the present solvent, are 'compatible' in limited range of PVC content in the blend.

### Morphology Studies

The morphology studies were performed using optical microscopy and SEM. Fig. 4 displays the results for the blend compositions (a) PVC/PS-80/20, (b) PVC/PS-60/40, (c) PVC/PS-30/70 (d) PVC/PS-20/80 and (e) PVC/PS-10/90 (f) PVC/PS-05/95 blends by optical microscopy. SEM images of the blend compositions (a) PVC/PS-80/20, (b) PVC/PS-60/40, (c) PVC/PS-30/70 (d) PVC/PS-20/80, and (e) PVC/PS-10/90 and (f) PVC/PS-05/95 are shown in Fig. 5.

From the Fig. 4, it can be seen that the PVC/PS binary

blends exhibit typical droplet-matrix morphology. The blend compositions (a) PVC/PS-80/20 and (b) PVC/PS-60/40 show that PVC is in the matrix phase and PS is dispersed in the PVC matrix. The lower concentration of PS shows tendency to remain phase separated and forming irregularly shaped, non uniformly distributed droplets in PVC matrix phase. The blend composition (c) PVC/PS-30/70 shows that though PVC becomes dispersed phase, non uniformity persists. For PVC/PS 20/80, 10/90 and 05/95 blend compositions, (d), (e) and (f) show that PVC forms uniform sized droplets as a dispersed phase in the matrix of PS. Also the droplets are dispersed uniformly in the matrix phase. Size of the droplets decreases with decrement in PVC content; and PVC gets dispersed more uniformly in the matrix phase PS.

The SEM study supports (Fig. 5) results shown by optical microscopy (Fig. 4). The blend composition PVC/PS-20/10, 10/90 and 05/95 show that the sizes of PVC droplets in dispersed phase are smaller, spherical and regularly arranged than those in other blends. The well defined boundaries of individual droplets of PVC show that there is no interaction between PVC and PS in the blend. The blend 'compatibility' is a relative term; and the domain size is often used to indicate the extent of mixing i.e. the smaller the domains are, the more 'compatible' the system. It is clear that blends with composition PVC/PS-80/20, 60/40 and 30/70 are 'incompatible', while PVC/PS-20/80, 10/90 and 05/95 show good mixing, uniform dispersion and homogeneity. Homogeneity improves as decrement in the PVC concentration in blends decreases the domain size of the dispersed phase, which is least for 05/95 leading to uniform distribution.

Thus at higher concentrations of PVC, the phase separation of PVC matrix phase and PS dispersed phase has led to observed two T<sub>g</sub>'s in blends. At lower concentrations of PVC in blends, the uniform distribution of uniform sized PVC droplets in a blend has led to increased 'compatibility' which has resulted in the observed single T<sub>g</sub>. Thus the morphological observations lend support to the results of thermal studies. Lack of polar group in PS impedes any intermolecular interaction in the PVC/PS blend, leading to immiscibility in such blends. 'Compatibility' of PVC/PS blend below 20wt% of PVC could be due to availability of free volume of homopolymer. Liu et al and Wu et al. have shown that miscibility can result due to gain in free volume. These studies suggested that in the absence of strong specific interactions between the chains of components forming the blend,

the miscibility can be affected by free volume of the homopolymer. Kumaraswamy and Ranaganathaihah have shown that PS has bigger free volume cavities ( $98.2 \text{ \AA}^3$ ) and more free volume fraction (31.6%) than the PVC ( $72.2 \text{ \AA}^3$ , 4.4%). Thus in a PVC/PS blend, when PVC is a minor phase, the free volume cavity of PS matrix phase can easily accommodate PVC minor

phase resulting in fine and easy dispersion of PVC. On the contrary, the PVC free volume cavity cannot accommodate PS even if PS is in minor phase. This view is well supported by Kumaraswamy and Ranaganathaihah who have shown that the free volume interaction parameter,  $\beta$  has been observed negative in less than 20wt% PVC composition, which is sign of 'compatibility' in a blend.

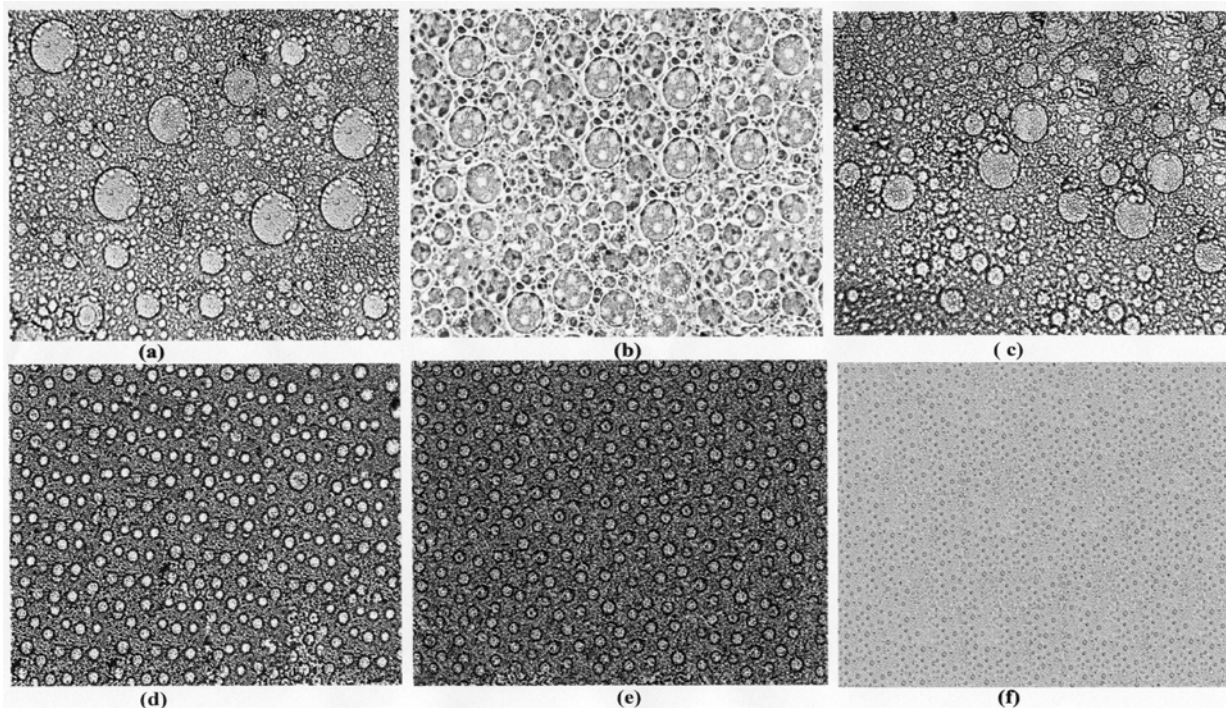


FIG. 4 OPTICAL MICROSCOPY PHOTOGRAPHS OF PVC/PS BLENDS FOR (a) 80/20, (b) 60/40, (c) 30/70 (d) 20/80 & (e) 10/90 (f) 05/95 COMPOSITIONS

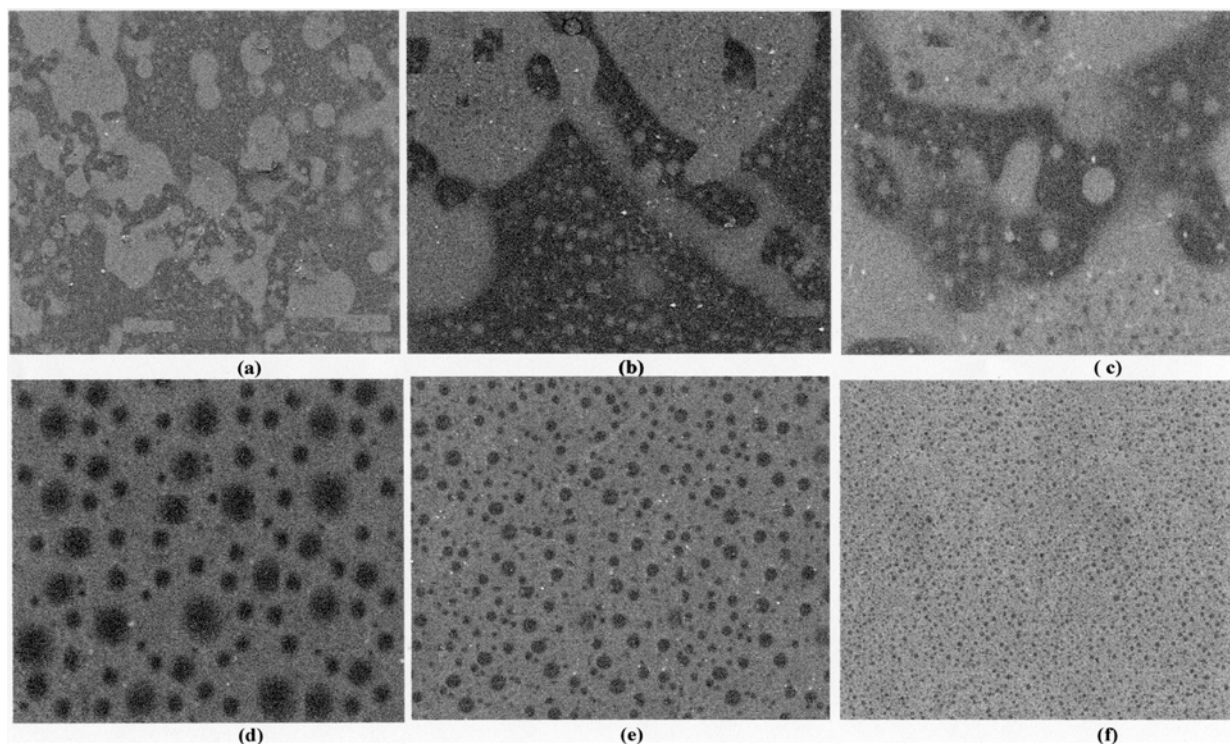


FIG.5 SEM IMAGES OF PVC/PS BLENDS FOR (a) 80/20, (b) 60/40, (c) 30/70 (d) 20/80, AND (e) 10/90 AND (f) -05/95 COMPOSITIONS

TABLE 1 THE APPARENT WEIGHT FRACTION DISSOLVED IN PS RICH PHASE AND PVC RICH PHASE.

Wt% of PS	Tg of PS (°C)	Tg of PVC (°C)	Fox equation				Woods Equation			
			PS rich phase		PVC rich phase		PS rich phase		PVC rich phase	
			w <sub>1</sub> '	w <sub>2</sub> '						
0		80								
10	92.7	80.4	0.745895	0.254105	0.027087	0.972913	0.705556	0.294444	0.022222	0.977778
20	93	80.9	0.761051	0.238949	0.060569	0.939431	0.722222	0.277778	0.05	0.95
30	93.4	81.4	0.781109	0.218891	0.093639	0.906361	0.744444	0.255556	0.077778	0.922222
40	93.8	81.9	0.800995	0.199005	0.126306	0.873694	0.766667	0.233333	0.105556	0.894444
50	94.2	82.4	0.820712	0.179288	0.158576	0.841424	0.788889	0.211111	0.133333	0.866667
60	94.7	82.8	0.845125	0.154875	0.184112	0.815888	0.816667	0.183333	0.155556	0.844444
70	95.1	83.3	0.86447	0.13553	0.215686	0.784314	0.838889	0.161111	0.183333	0.816667
80	95.3	83.8	0.874082	0.125918	0.246884	0.753116	0.85	0.15	0.211111	0.788889
100	98									

**Polymer-Polymer Interaction Parameter Calculated from Glass Transition Temperature Measurement.**

Theoretically, Tg of the miscible polymer blend can be estimated empirically using Fox eq<sup>n</sup>. and Wood's eq<sup>n</sup> (which is given in the thermal study) by substituting the individual components' Tgs and their weight percentages in the blend. When the two polymers which are partially miscible are blended, there is stabilization in two phases at the end of mixing process, of which one is rich in polymer 1 (Phase 1) and the other dominated by polymer 2 (Phase 2). Each of these phases may be considered as totally miscible system, as no further phase separation occurs once the equilibrium has been reached; hence Fox's or Wood's eq<sup>n</sup> are applicable to each of them, so as to quantify the portion of each component in blend. The Fox eq<sup>n</sup> (4) and Woods eq<sup>n</sup> (5) give the extent of component mixing for PVC/PS blends.

$$w_1' = \frac{Tg_1(Tg_{1,b} - Tg_2)}{Tg_{1,b}(Tg_1 - Tg_2)} \tag{4}$$

$$w_1' = \frac{(Tg_{1,b} - Tg_2)}{(Tg_1 - Tg_2)} \tag{5}$$

where w<sub>1</sub>' is the weight fraction of the PS in PS phase, w<sub>2</sub>' = 1 - w<sub>1</sub>' is the weight fraction of PVC in PS phase. Tg<sub>1,b</sub>, is the observed Tg of the PS rich phase in the blends, and Tg<sub>1</sub>, Tg<sub>2</sub> are Tg's of homopolymer 1 and 2 respectively.

The volume fraction can be calculated via the following ratios

$$\phi_1' = \frac{\frac{w_1'}{\rho_1}}{\frac{w_1'}{\rho_1} + \frac{w_2'}{\rho_2}} \tag{6}$$

and

$$\phi_2' = 1 - \phi_1'$$

where φ<sub>1</sub>', φ<sub>2</sub>', ρ<sub>1</sub> and ρ<sub>2</sub> are the volume fractions

and the densities of PVC and PS in the PVC phase respectively.

The Flory-Huggins polymer-polymer interaction parameter χ<sub>12</sub> is determined by applying the expression developed by Kim and Burns.

$$\chi_{12} = \frac{\ln\left(\frac{\phi_1''}{\phi_1'}\right) + \left(1 - \frac{m_1}{m_2}\right)(\phi_2'' - \phi_2')}{m_1(\phi_2'^2 - \phi_2''^2)} \tag{7}$$

where, m<sub>1</sub> and m<sub>2</sub> are degrees of polymerization for PS and PVC respectively.

Table (1) shows the apparent weight fraction dissolved in PS rich phase and PVC rich phase. The weight fraction of PVC (w<sub>2</sub>') dissolved in PS rich phase is higher than PS (w<sub>1</sub>') dissolved in PVC rich phase, which confirms that the uniform dispersion of PVC in PS matrix is easily possible; however PS dispersion in PVC matrix is difficult.

TABLE 2 THE INTERACTION PARAMETER CALCULATED FROM FOX EQUATION AND WOOD'S EQUATION.

Wt% of PS	Interaction Parameter		
	Fox equation (χ <sub>12</sub> )	Woods Equation (χ <sub>12</sub> )	At critical point (χ <sub>12</sub> ) <sub>c</sub>
10	0.0033	0.0033	0.0017
20	0.0026	0.0026	0.0017
30	0.0023	0.0023	0.0017
40	0.0022	0.0021	0.0017
50	0.0020	0.0020	0.0017
60	0.0020	0.0019	0.0017
70	0.0019	0.0019	0.0017
80	0.0018	0.0018	0.0017

The interaction parameter calculated from eq<sup>n</sup> (7) is shown in Table (2). The values of χ<sub>12</sub> are from 0.0018 to 0.0033. The interaction parameter at critical point (χ<sub>12</sub>)<sub>c</sub> can be derived easily from degrees of polymerization. This value can serve as criterion for predicting phase separation of a blend. The (χ<sub>12</sub>)<sub>c</sub> can be calculated by using equation

$$(\chi_{12})_c = \frac{1}{2} (m_1^{-1/2} + m_2^{-1/2})^2 \quad (8)$$

The value of  $(\chi_{12})_c$  was found to be 0.0017 for PVC/PS blends. It can be surmised that if  $\chi_{12} < (\chi_{12})_c$  then the polymers are miscible with each other (no phase separation). On the other hand, if  $\chi_{12} > (\chi_{12})_c$  in the blends, phase separation can occur.

Fig. 6 shows the relation between  $\chi_{12}$  and the weight fraction of PS in PVC/PS blends. The interaction parameter  $\chi_{12}$  decreases with increase in the weight fraction of PS. It shows that 'compatibility' will increase more in the region of PS rich composition than the PVC-rich composition in the PVC/PS blends. All values of  $\chi_{12}$  are greater than  $(\chi_{12})_c$ . This interaction is probably enough to get high degree of homogeneity; but a blend is not miscible on the molecular level. Thus this study establishes that as PS concentration increase in the blend, the PVC/PS blend approaches 'compatibility'.

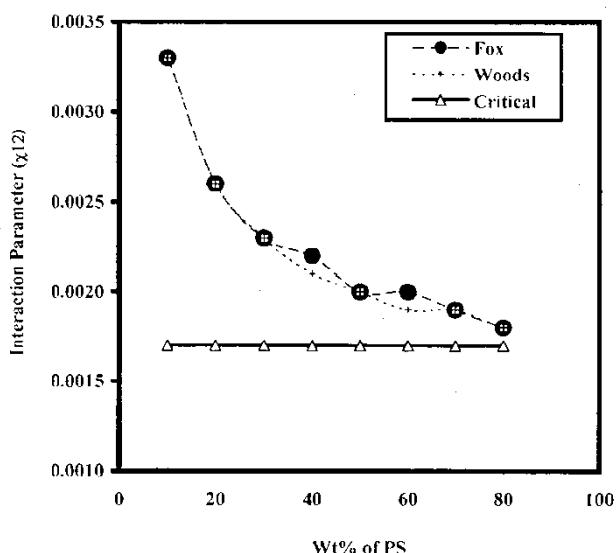
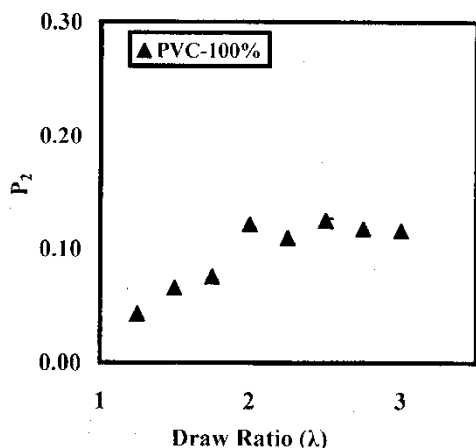


FIG. 6 THE RELATION BETWEEN INTERACTION PARAMETER AND THE WEIGHT FRACTION OF PS IN PVC/PS BLENDS.



## FTIR Studies/Infrared Dichroism

### 1) Peak Assignment

In order to study chain orientation in polymer blend by linear infrared dichroism, it is necessary that each component polymer has a characteristic absorption band at frequencies where absorbance of the other component is nearly zero. Fig. 7 shows the infrared spectra of pure PVC and pure PS from 4000 cm<sup>-1</sup> to 450 cm<sup>-1</sup>. PVC band at 960 cm<sup>-1</sup> which represents CH<sub>2</sub> rocking mode and PS band at 1028 cm<sup>-1</sup> which represents CH bending mode of the aromatic ring were chosen for the study. Both bands have angle  $\alpha$  (the angle between dipole moment vector and chain axis) as 90°.

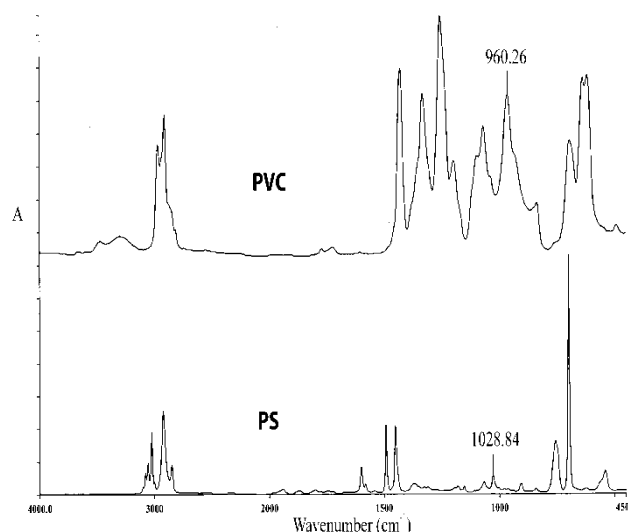


FIG. 7 INFRARED SPECTRUMS OF PURE PVC AND PS

### 2) Orientation Studies

Fig. (8) shows plots of orientation function with draw ratio for pure PVC and pure PS films. The blend films of PVC/PS with compositions (a) 80/20 (b) 60/40 (c) 30/70 (d) 20/80 (e) 10/90 and (f) 05/95 are shown in Fig (9).

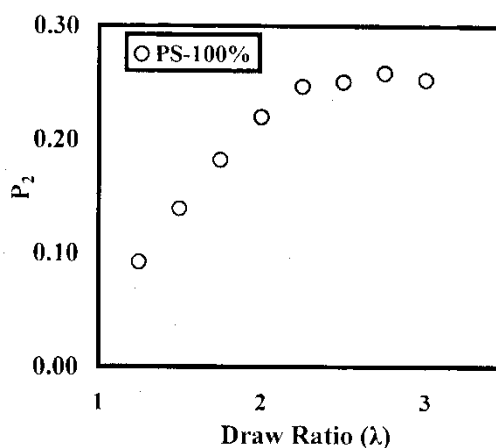


FIG. 8 VARIATION OF ORIENTATION FUNCTION (P<sub>2</sub>) WITH DRAW RATIO (λ) For (a) PVC-100% AND (b) PS-100%

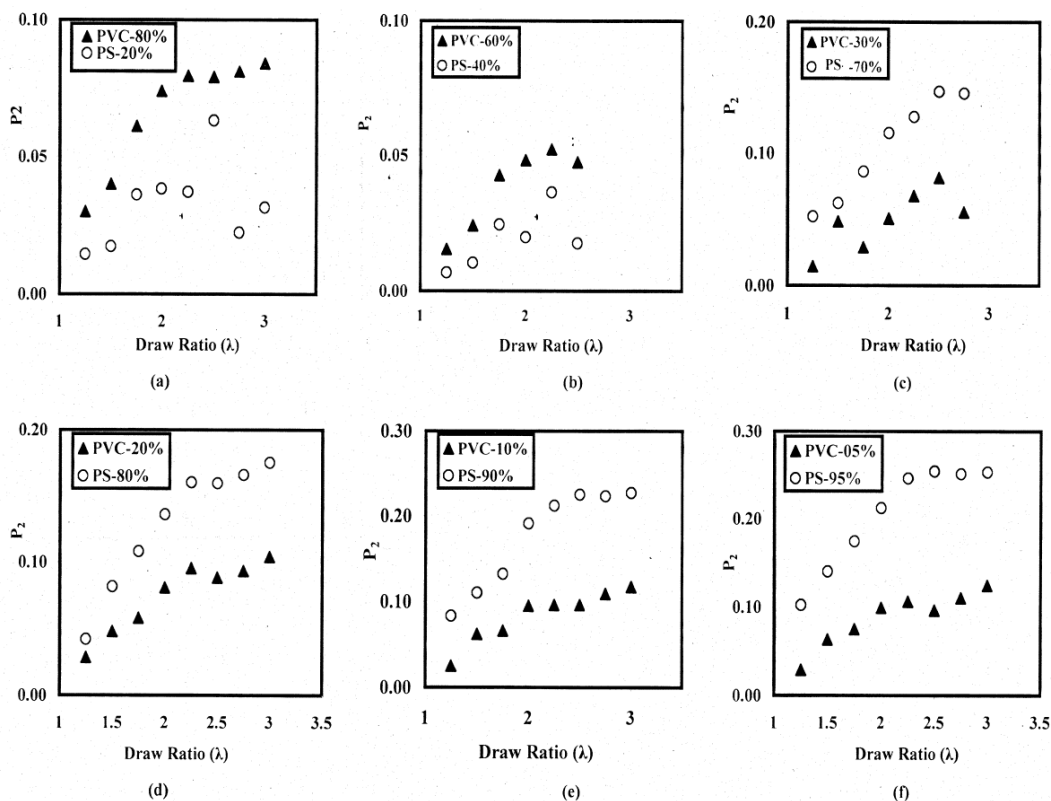


FIG. 9 VARIATION OF ORIENTATION FUNCTION ( $P_2$ ) WITH DRAW RATIO ( $\lambda$ ) FOR PVC/PS BLENDS.

The orientation behaviour in pure PVC and pure PS shows that PVC chains orient less than PS chains. As  $T_g$  of PVC ( $80^\circ\text{C}$ ) is lesser than that of PS ( $98^\circ\text{C}$ ); PVC chains relax more rapidly than the PS chains at the stretching temperature ( $120^\circ\text{C}$ ), which has resulted in less orientation of PVC compared to PS. Generally, magnitude of orientation function increases with increase in draw ratio attains a plateau at certain draw ratio.

As shown in Fig. (9), the blend PVC/PS-80/20, 60/40 and 30/70 compositions show that the major components orient linearly to larger extent compared to minor dispersed component. This is in agreement with the results obtained by other authors. The blend PVC/PS-20/80, 10/90 and 05/95 compositions show that though PS, the major component PS, the orientation behaviour of PVC and PS in blends is very similar to pure PVC and pure PS.

Fig. (10) shows the variation of the orientation function with draw ratio for PVC and PS, in blends at various PS concentrations. The slope at the origin  $\frac{d\langle P_2(\cos \theta) \rangle}{d\lambda}$  was calculated from the experimental curves for each composition assuming a linear variation of the orientation

function, which is reasonable for small draw ratios. The orientation behaviour shows that the major component in the blend orients more than the dispersed phase as the major part of the applied stress is taken up by the major component. However, the orientation is less than the pure polymer. This may be attributed to the resistance offered to the chain mobility of major component during orientation by the presence of the minor phase polymer. The orientation behaviour of PVC in less than 20wt% is very similar to pure PVC.

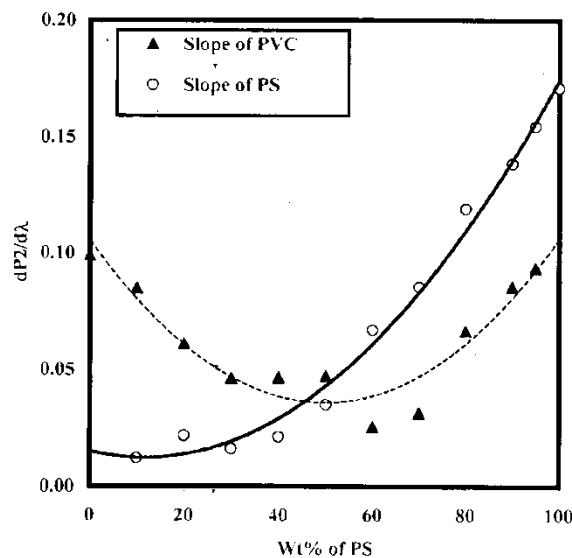


FIG. 10 THE VARIATION OF THE ORIENTATION FUNCTION i.e.

$(\frac{dP}{d\lambda})$  WITH STRETCHING RATIO FOR PVC AND PS, AT VARIOUS PS CONCENTRATIONS

The results obtained for PVC/PS blends can be interpreted in terms of larger free volume cavities in PS and lack of interaction between PVC and PS. The minor phase PVC chains accommodate easily in PS matrix phase as PS has larger free volume. As the orientation behaviour of PVC in these blends is very similar to pure PVC, it suggests that chain hindrance for PVC chains remains the same as in pure in these blends implying that there is no force acting on PVC due to the presence of PS in the blend. This clearly indicates that there is no specific interaction and hence no miscibility at the molecular level for these blends; but components homogeneously mix; and mixing improves with lesser and lesser quantities of PVC in the blend, in addition, trend and values of orientation function of PVC in blend approach to that of pure PVC trend and values. The result is supported by microscopy studies which show sharp boundaries of uniformly sized PVC droplets and uniform distribution of these droplets in the blend compositions PVC/PS-20/80, 10/90 and 05/95.

Thus orientation studies also suggest high degree of homogeneity due to uniform distribution of PVC dispersed phase in PVC/PS blends with 20 wt% and less PVC content leading to 'compatibility' in the PVC/PS blend.

**Mechanical Studies**

The mechanical properties of blends highly depend on the factors like miscibility of the blends, molecular weight, morphology and molecular orientation [47-48]. Hence the mechanical properties of PVC/PS blend were studied using the storage modulus near room temperature for various blend compositions. The tensile strength of pure PVC, PS and PVC/PS blends was studied for stretched samples at room temperature.

**1) Storage Modulus (E')**

Fig. (11) shows the variation of storage modulus (E') near room temperature for various blend compositions.

The pure polymers PVC and PS have the values of storage moduli 2.33 and 2.24 GPa, respectively, at room temperature. These values show marginal increment in the blend less than 20wt% PVC composition. This trend of the mechanical

behaviour is observed in the PVC/PS blend composition only when the two polymeric phases are distributed uniformly. However, as the two phases are heterogeneously distributed in more than PVC-20 wt% composition, the mechanical properties of such PVC/PS blends decrease.

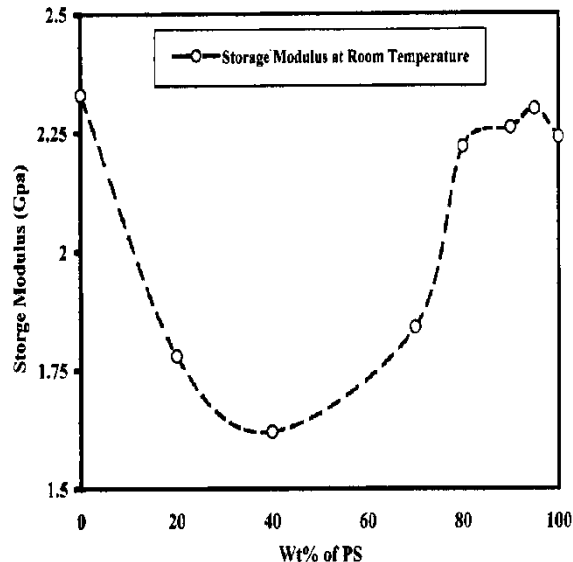


FIG. 11 THE STORAGE MODULUS (E') OBTAINED FOR PURE PVC, PS AND THEIR BLEND COMPOSITIONS AT ROOM TEMPERATURE.

Thus the 'compatibility' observed in the composition less than PVC-20wt% in the blend is reflected in the mechanical behaviour of PVC/PS blends.

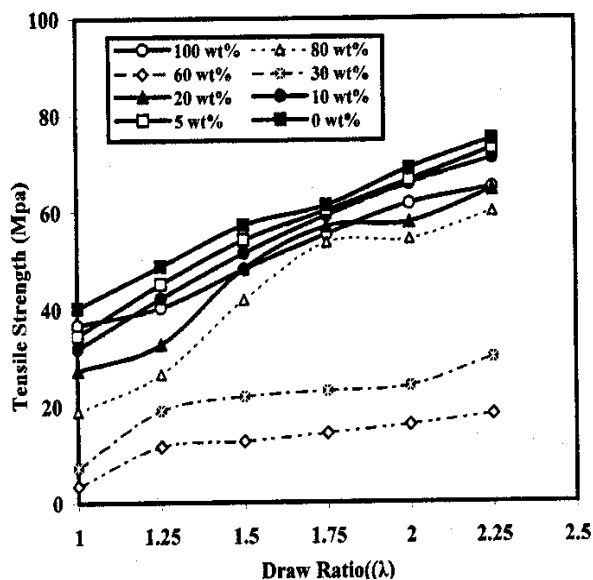


FIG. 12 TENSILE STRENGTH OBTAINED FOR STRETCHED SAMPLES OF PURE PVC, PS AND THEIR BLEND COMPOSITIONS AT ROOM TEMPERATURE.

**2) Tensile Strength**

Fig. (12) shows a plot of tensile strength with various draw ratios for stretched pure PVC, pure PS and PVC/PS blends with different compositions.

Generally tensile strength is increasing with draw ratio. The PVC/PS-20/80, 10/90 and 05/95 blend compositions show better tensile strength than pure PVC for all draw ratios.

At temperature higher than  $T_g$ , the chain mobility is higher. Also for PVC/PS 'compatible' blends, i.e. at lower PVC concentrations in the blend, due to availability of free volume to PVC chains, higher chain mobility is possible hence more chains than in other blends as well as in pure PVC will be easily oriented in a stretching direction leading to higher tensile strength. At lower concentrations of PVC (20wt% and less), homogeneity of the two phases has led to the 'compatibility' of the blends and hence the increase in tensile strength of these blends compared to other blends and pure PVC. However, if they are heterogeneously distributed then hindrance to chain mobility will reduce the values of orientation and hence decreasing the tensile strength the constituent polymers can attain. When PVC is in matrix phase, available free volume also is less, leading to additional chain-hindrance. Hence mechanical properties are inferior as being observed for the blends with the concentrations more than 20wt% of PVC.

## Conclusions

Pure PVC, PS and PVC/PS blends in various compositions were studied using thermal, Microscopy, Infrared Spectroscopy and UTM techniques. Thermal study shows that 'compatibility' is observed in the limited composition of PVC/PS blend; blend with PVC concentration 20wt% and below show 'compatibility'. The use of equation proposed by Kim and Burns confirmed that  $\chi_{12}$  has positive and very low value, which indicates that there has moderate interaction which is enough to get high degree of homogeneity in the blend. It was also suggested that low values of concentrations of PVC in the blend favour higher degree of homogeneity. Optical microscopy and SEM studies revealed that for the concentrations of PVC-20wt% and less in the blends, the distribution of PVC dispersed phase in PS matrix is uniform though well defined boundaries of individual droplets of PVC show that there is no interaction between PVC and PS components. This indicates that though these blends are immiscible at the molecular level their blending is homogeneous for these compositions and can be treated as 'compatible' blends. Orientation studies indicated that the matrix phase orients more than the

dispersed phase. The dispersed phase of PVC in PVC/PS-20/80, 10/90 and 05/95 blend composition orients equivalent to PVC in pure film confirming the homogeneity of the blends. The synergistic behavior of storage modulus observed for the blends containing less than PVC-20wt% blend confirms that two phases are distributed uniformly in these blends. PVC/PS-20/80, 10/90 and 05/95 blends show superior mechanical properties by way of higher tensile strength values than the other blends. This can be explained on the basis of 'compatibility' (by way of uniform distribution and availability of larger free volume) which will give less chain hindrance and produce greater orientation in the direction of stretching, leading to higher tensile strength. Thus it was concluded that the 'compatibility' observed in PVC/PS blend is due to the phase morphology, which controls the final orientation and mechanical behaviour of these blends.

## REFERENCES

- Abd-El-Messieh S.L., *Polym.-Plastics Tech. and Engg.* 2003, 42,153.
- Abtal E., *Polym. Engg. Sci*, 1992, 32, 1857.
- Acosta J.L., Linares A. *J. Appl. Polym. Sci.* 1998, 67,997.
- Ahmad Z., Al-Awadi N.A. *Polym. Degradation and Stability* 2007,92,1025.
- Bower D.I., King J., Maddams W.F. *J. Macromol. Sci. Phys.* 1981, B20, 305.
- Chabot P., Prudhomme R., Pezolet M. *J. Polym. Sci Part B: Polym. Phys.* 1990, 28, 1283.
- Chun Y.S., Lee H.S., Kim W.N. *Polym. Engg. Sci.* 1996, 36,2 694.
- Chun Y.S., Lee H.S., Kim W.N., Yoon H.G. *J. Appl. Polym. Sci.* 2000,78,2488.
- Deshpande V.D., Singh U. *J. Appl. Polym. Sci.* 2006,101, 624-630.
- Eboatu A.N., Olojo D.O. *J. Appl. Polym. Sci.* 1989,37,2485.
- Endo S., Min K., White J.L. *Polym. Engg. Sci*, 1986, 26, 45.
- Fekete E., Foldes E., Damsits F. *Polym. Bulletin*, 2000, 44,363.
- Fox T.G. *Bull. Am. Phys. Soc*, 1965, 1,123.
- Haba Y., Narkis M. *Polym. Engg. Sci.* 2004,44,1473.
- Hamon L., Grohens Y., Soldera A. *Polym.* 2001,42,9697.
- Hibi S., Maeda M., Kubota H., Miura T. *Polym.* 1977, 18, 137.
- Hubbell D.S., Cooper S.L. *J. Polym. Sci, Polym. Phys. Ed.* 1977, 15, 1143.

- Jasse B., Konig J.L. J. Polym. Sci. 1979, 17,799.
- Kajima S., Porter R.S. J. Polym. Phys. Ed. 1978, 16, 1729.
- Karam H.J. Polymer 'compatibility' and 'Incompatibility', Vol.2. Switzerland: MMI Press Sympo. Series, 1982 p.93.
- Keroacka D., Zhao Y., Prud'homme R. Polym. 1998, 40, 243.
- Kim J.H., Karasz FE, Malone M.F. Polym. Engg. Sci. 1991, 31,981.
- Kim W.N., Burns C.M. J. Appl. Polym. Sci, 1990,41,1575.
- Kim W.N., Burns C.M. J. Polym. Sci. Part B: Polym. Phys. 1990, 28, 1409.
- Kim W.N., Burns C.M. Macromolecules, 1987,20,1876.
- Kumaraswamy G.N., Ranganathaiah C. Polym. Engg. Sci. 2006, 46, 1231.
- Kwak S.Y., Kim S.H., Suzuki T. Polym. 2004, 45, 8153.
- Lee H.S., Kim W.N., Burns C.M. J. Appl. Polym. Sci. 1997,64,1301.
- Lefebvre D., Jasse B., Monnerie L. Polym. 1984, 25, 318.
- Li D., Brisson J. Macromolecules, 1997, 30,8425.
- Liu J., Jean Y.C., Yang H. Macromolecules 1995, 28, 5774.
- Li W., Prud'homme R.E. Polym. 1994, 35, 3260.
- Lu F.J., Burchell D.J., Li X. Polym. Engg. Sci., 1983, 23,861.
- Peterlin A. Polym. Engg. Sci. 1979, 19,118.
- Rao R.V., Ashokan P.V. Asian J. of Chem. 1996,8,13.
- Rider G.J., Hargreaves E.J. Physics D. 1970, 3, 993.
- Robinson M.E.R., Bower D.I., Maddams W.F. J Polym. Sci. Polym. Phys. Ed. 1978, 16, 2115.
- Samules R.J. Structured polymer Properties, Wiley, New York, 1974.
- Shindo Y., Read B.E., Stein R.S. Macromol. Chem. 1968, 118, 272.
- Springer H., Neuert R., Miller F.D. and Hinrichsen G. Colloid and Polym. Sci 1983, 261, 800.
- Tabb D.L., Koenig J.L. Macromolecules 1975, 8, 929.
- Theodorou M., Jasse B. J. Polym. Sci. 1983, 21, 2263.
- Ward I.M. Applied Science Publications, London, 1975.
- Wood L.A. J. Polym. Sci. 1958, 28,319.
- Wu S.J. J. Polym. Sci. Part B: Polym. Phys. 1987,25,2511.
- Zhong Z., Zheng S., Yang K., Guo Q. J. Appl. Polym. Sci. 1998, 69, 995.
- Zhong Z., Zheng S., Yang K., Guo Q. J. Appl. Polym. Sci. 1998, 69, 995.

# Formation of Nanospheres and Nanorods of Titanium Dioxide in a Low-pressure Ar/O<sub>2</sub> Plasma Controlled by a Sputtering Method

Yousuke Yamazaki, Satoru Iizuka\*

Department of Electrical Engineering, Tohoku University  
Aramaki Aza-Aoba 6-6-05, Aoba-ku, Sendai 980-8579, Japan

\*iizuka@ecei.tohoku.ac.jp

## Abstract

Formation of nanoparticles and nanorods of titanium dioxide (TiO<sub>2</sub>) in Ar/O<sub>2</sub> plasma was investigated by controlling the discharge parameters, such as partial pressure and applied voltage. The nanostructures were produced by reactions of oxygen with titanium atoms, sputtered from a titanium target by reactive sputtering. The deposits were analysed by the SEM, TEM and EDX. Many nanospheres were observed on thin films composed of nanorods, deposited on a silicon substrate at an applied voltage from 1,500 to 3,000 V and a total pressure of 0.5 Torr with a deposition time of 1.5 h. These properties were nearly independent of the partial pressure ratio of oxygen to argon. The diameter of the nanospheres varied from 15 to 100 nm. The thin film quality was controllable by adjusting the electric discharge conditions.

## Keywords

*Titanium Dioxides; Nanospheres; Nanorods; Plasma Sputtering Method*

## Introduction

Titanium dioxide (TiO<sub>2</sub>) is well known as a semiconductor with a wide band gap of 3.2 eV at room temperature; and thus it is expected to be useful as an electrode material of solar cells to improve the efficiency. Superior photochemical properties of TiO<sub>2</sub> are also applied to the photochemical reaction of the electrode of dye-sensitized solar cells. Its photocatalytic effect will also be applicable to environmental problems. Application to medical treatments such as the self-cleaning effect, purification, sterilization, and deodorization has also been considered. TiO<sub>2</sub> typically has two crystallites, i.e., anatase and rutile. The former is useful for photoactivities and the latter is widely used as white dye powder. Several types of TiO<sub>2</sub> nanostructures have been reported, such as baroques, nanorods, nanowires, and thin films. If a solar cell electrode

consists of TiO<sub>2</sub> nanospheres, the surface electrode area for photochemical reaction will become larger, which may lead to an increase in electric power generation. For this reason, spherical TiO<sub>2</sub> particles have attracted attention for application to the electrodes of dye-sensitized solar cells.

In this study, the creation of nanospheres and nanorods of TiO<sub>2</sub> was controlled by changing the experimental conditions such as discharge power and mixing ratio of oxygen to argon under the fixed total pressure of working gases of Ar and O<sub>2</sub>.

## Experimental Setup

Figure 1 shows the entire experimental configuration. The small coaxial electrode system consisted of a plate electrode and an inner electrode inserted into a narrow glass tube. The inner electrode was made of a titanium rod with diameter of 2 mm. The outer plate electrode made of titanium was not fixed, so the distance between the two electrodes could be varied. In this experiment, however, the distance between the top of the inner electrode and the outer electrode was fixed at 15 mm. For film deposition, a substrate made of Si was placed on the grounded plate electrode.

The entire electrode system shown in Figure 1 was set inside a cylindrical vacuum chamber 50 cm in diameter and 20 cm in height. The working gases of Ar and O<sub>2</sub> were independently introduced into a mixing vessel through mass flow controllers, and finally the mixed gas was fed into the discharge region through a gas inlet tube connected to the inner electrode, as shown in Figure 1. The outgoing gas from the discharge region was directly drained into the chamber and evacuated by a rotary pump. Since the length of the glass tube and the glass plate was small (~10 mm), the pressure in the discharge region was nearly as much as that in the vacuum chamber.

Typically, the gas flow rate ratio of argon to oxygen was varied from  $\text{Ar}/\text{O}_2 = 0/1$  to  $\text{Ar}/\text{O}_2 = 1/0$  under a total pressure of Ar and  $\text{O}_2$  fixed at 0.5 Torr.

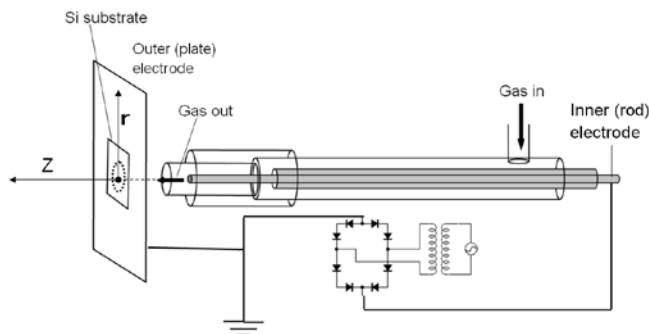


FIG. 1 EXPERIMENTAL APPARATUS. PLASMA DISCHARGE OCCURRED BETWEEN A ROD ELECTRODE AND A PLATE THAT WAS GROUNDED ELECTRICALLY. THE PLATE ELECTRODE WITH A HOLE 12 MM IN DIAMETER WAS USED FOR EXPOSING THE SI SUBSTRATE TO THE PLASMA. THE GENERATED PARTICLES, CARRIED BY THE FLOW OF GAS, WERE DEPOSITED ON THE SI SUBSTRATE.

Rectified DC voltage of an amplified commercial power source was directly supplied to the inner electrode through a coaxial cable, while the outer plate electrode was grounded. The commercial power supply provided a sinusoidal waveform with a period of 20 ms, i.e., 50 Hz. The applied voltage could be increased up to 6,000 V.

The properties of the plasma were mainly measured by a Langmuir probe. The tip of the probe was a stainless steel rod 2 mm in length and 1 mm in diameter. The probe could be shifted in the axial and the radial directions. The surface morphology was analyzed by a scanning electron microscope (SEM) and a transmission electron microscope (TEM). The atomic component of the deposited films was analyzed by an energy dispersive X-ray spectroscopy (EDX) installed in the SEM system.

Using this system, the discharge parameters such as flow rate ratio  $\text{Ar}/\text{O}_2$  and applied voltage could be changed. The DC discharge took place between the tip of the titanium electrode and the titanium plate electrode with a hole at the centre. In this experiment the partial pressure ratio and supplied voltage were selected as a parameter.

## Results and Discussion

### Plasma Parameters

Firstly, the plasma parameters such as electron density and electron temperature in the axial  $z$  and the radial  $r$  directions were measured in a pure argon plasma. The plasma flowed through the hole of the substrate

holder toward the backside. Here, the origin of the radial and axial coordinates was set at the center of the hole of the substrate holder, as shown in Fig. 1. The electron density had a maximum at the radial center ( $r = 0$ ) and decreased in the radial direction. Apart from the substrate plate, the electron density rapidly decreased and became almost zero at 4 mm in the axial  $z$  direction. On the other hand, the electron temperature  $T_e$  was almost changeless both in the radial and axial directions. The electron temperature was kept almost constant at about 3 eV. The plasma profiles were not much changed by the applied voltage  $V_d$ . The electron density, however, was increased with  $V_d$  although it was almost saturated in the range of  $V_d$  larger than 3,000 V. The electron temperature was also not much changed by the applied voltage.

The effect of oxygen on the radial profiles of the electron temperature  $T_e$  and on the electron density  $n_e$  is shown in Figs. 2(a) and (b), respectively. Basic properties were almost the same as those of the pure argon plasma. As shown in Fig. 2(b), the density profile had a maximum at the radial center. However, with an increase of oxygen ratio the plasma density increased and became almost saturated when the oxygen ratio was raised above 50%. Concerning the electron temperature profile, a quite homogeneous profile was obtained, as shown in Fig. 2(a). However, the electron temperature decreased from 3.5 eV to 2 eV with the increase of the oxygen ratio from 0% to 100%. Relatively low electron temperature plasma was produced when oxygen was introduced. This might have an effect on the reaction for producing molecules of  $\text{TiO}_2$ . By adding oxygen, the plasma shrank more and hardly existed in the regions  $z$  greater than 20 mm and  $r$  greater than 5 mm.

From the plasma parameter measurement the plasma was found to spread in the shape of a cone. Apart from the electrode, electron density rapidly became small, while the electron temperature profile remained almost uniform.

### Nanosphere and Nanorod Deposition

To control of the nanostructures of  $\text{TiO}_2$  thin films, we investigated how the film quality would change when the plasma parameters were changed. Figure 3 shows SEM images of the surface of the Si substrate. Spherical nanoparticles, i.e., nanospheres, were clearly deposited on the Si substrate regardless of the  $\text{Ar}/\text{O}_2$  ratio. When the partial pressure ratio of  $\text{Ar}/\text{O}_2$  was

increased, however, the nanospheres tended to become large. Contrarily, the diameter of the particles became small when the pure oxygen plasma was employed. The cause was thought to be as that the surface of titanium electrode was covered with oxide film of TiO<sub>2</sub> in the case of high partial pressure of oxygen. Also, the increase of oxygen in the plasma might have brought about a decrease of ion sputtering rate by decreasing the amount of argon. Additionally, the electron temperature decreased in the case of oxygen-dominated plasma, as shown in Fig. 2(a). These occurrences might result in a decrease in amount of Ti atom emission into the plasma, together with a decrease in dissociation of oxygen molecules.

Therefore, the chemical reaction between Ti and O\* would be more or less suppressed, which might cause a reduction of TiO<sub>2</sub> cluster formation. Thus, the particle size might decrease due to a decrease in the amount of coagulation of TiO<sub>2</sub> nanoclusters.

The variation of particle size was plotted as a function of the flow-rate ratio of Ar/O<sub>2</sub> in Fig. 4. The particle size had a minimum at Ar/O<sub>2</sub> = 0 %, where the average size was about 15 nm. With an increase in the Ar/O<sub>2</sub> ratio, the particle size gradually increased and attained to 100 nm. From these results it was found that the particle size could be controlled in the range of 15 to 100 nm by changing the gas flow rate ratio of Ar/O<sub>2</sub>.

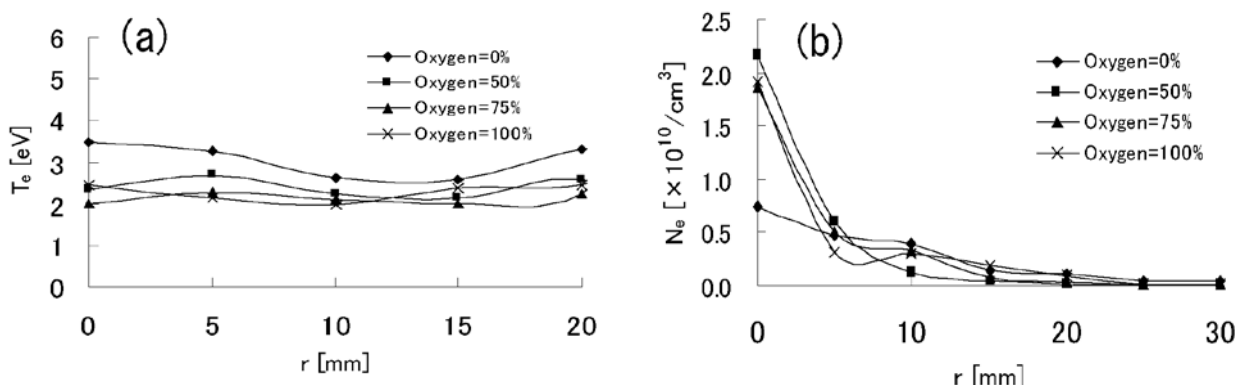


FIG. 2 PROFILES OF (A) ELECTRON TEMPERATURE  $T_e$  AND (B) ELECTRON DENSITY  $N_e$  IN THE RADIAL DIRECTION WITH OXYGEN TO ARGON RATIO AS A PARAMETER.  $N_e$  INCREASED WHEN OXYGEN WAS INTRODUCED.  $N_e$  PROFILE, HOWEVER, SHRUNK MUCH MORE.  $T_e$  PROFILE WAS ALMOST UNIFORM, BUT  $T_e$  DECREASED WHEN OXYGEN WAS INTRODUCED.

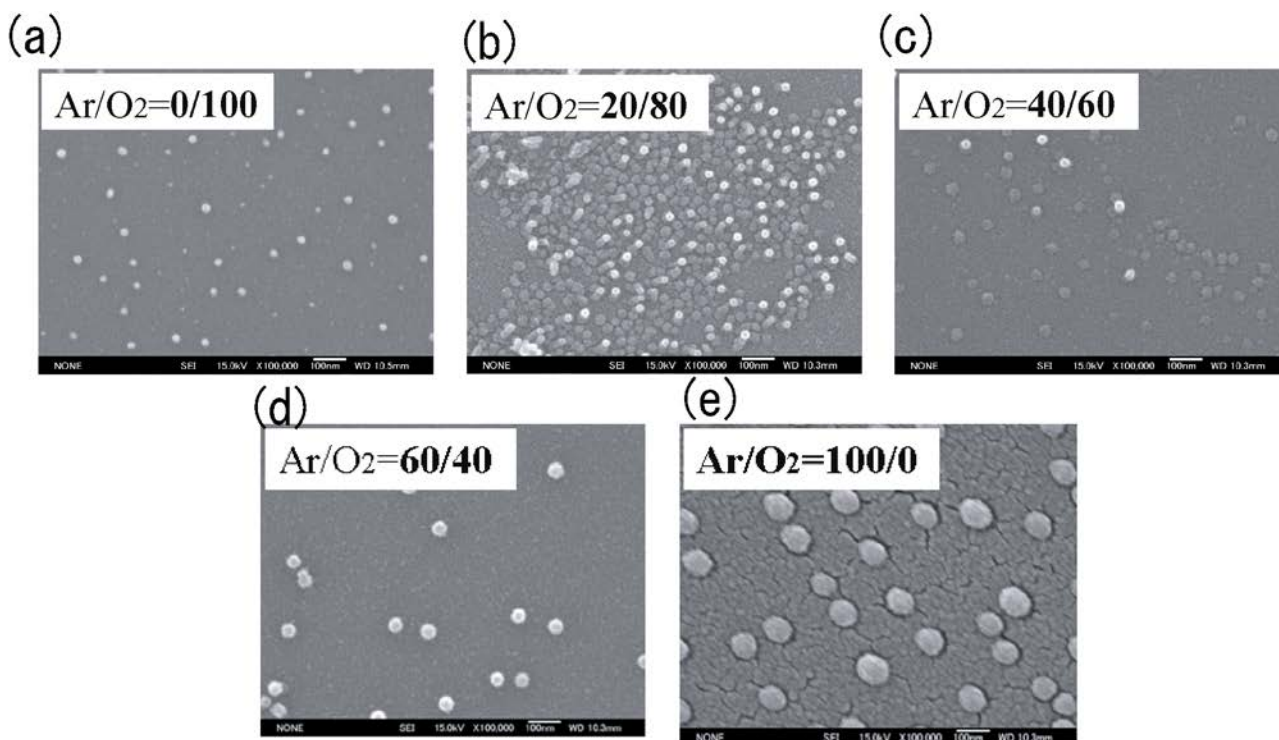


FIG. 3 SEM IMAGES OF NANOSTRUCTURES DEPOSITED ON THE SI SUBSTRATE WITH THE GAS FLOW RATE RATIO AR/O<sub>2</sub> AS A PARAMETER. THE PARTICLE SIZE OF NANOSPHERES INCREASED WITH INCREASING AR/O<sub>2</sub> RATIO. ALL THE MAGNIFICATIONS OF SEM IMAGES ARE 10,000 AND THE SCALE BAR IS 100 NM IN LENGTH.

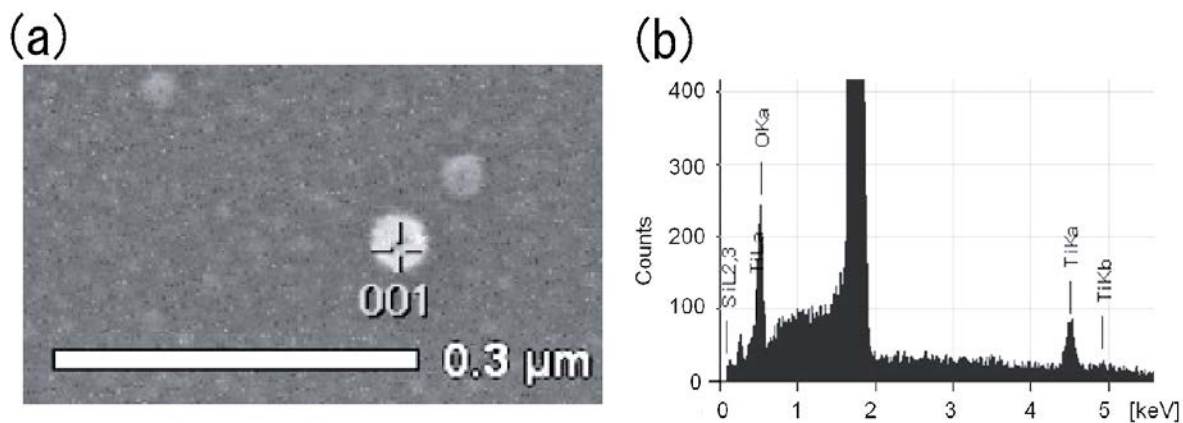


FIG. 5 SEM IMAGE OF NANOSPHERE AND (B) ITS EDX SPECTRUM. THE SPHERICAL PARTICULATES WERE COMPOSED OF TITANIUM AND OXYGEN. THE STRONG PEAK AT ABOUT 1.8 KEV WAS A SIGNAL FROM SI THAT CAME FROM THE SI SUBSTRATE

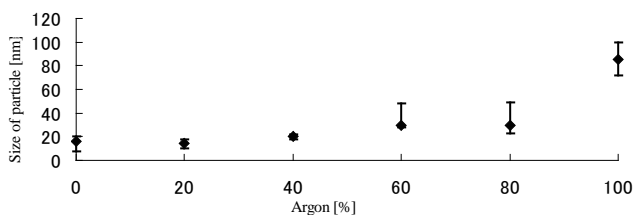


FIG. 4 AR/O<sub>2</sub> PARTIAL PRESSURE DEPENDENCE OF THE SIZE OF NANOSPHERES. THE PARTICLE SIZE HAD A MINIMUM AT AR/O<sub>2</sub> = 0 %, WHERE THE SIZE WAS ABOUT 15 NM. WITH INCREASING AR/O<sub>2</sub> RATIO, THE PARTICLE SIZE ATTAINED TO 100 NM. THEREFORE, THE PARTICLE SIZE COULD BE CONTROLLED BY ADJUSTING THE AR FLOW RATE RATIO.

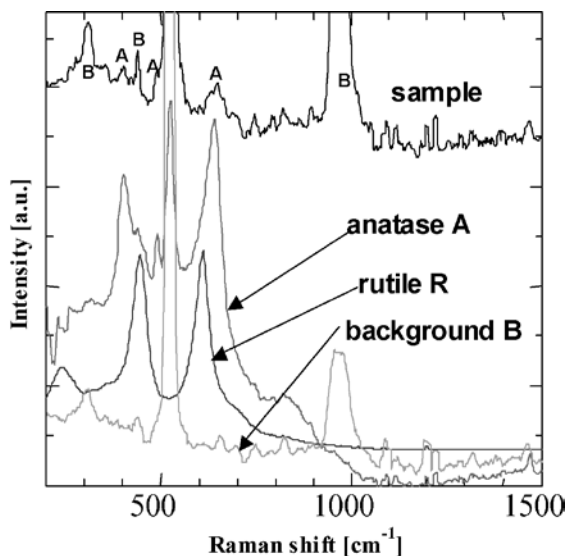


FIG. 6 RAMAN SPECTRA OF DEPOSITED SAMPLE, ANATASE SAMPLE, RUTIL SAMPLE, AND BACKGROUND SI SUBSTRATE. PEAKS CORRESPONDING TO ANATASE AND BACKGROUND ARE DENOTED BY "A" AND "B", RESPECTIVELY. NO PEAK CORRESPONDING TO RUTILE WAS FOUND.

In order to identify the atomic composition of such nanospheres, EDX analysis was carried out. The SEM image in Fig. 5(a) shows a typically spherical particle, which was subjected to EDX analysis as shown by the spectrum in Fig. 5(b). Both titanium and oxygen were detected together with intense signals coming from the Si substrate. No other atomic species were detected as

contamination in the nanospheres. From this result, it was confirmed that the nanospheres only consisted of titanium and oxygen. Figure 6 shows Raman spectra of the deposited sample, standard anatase sample, standard rutile sample, and background Si substrate. Many peaks were observed in the spectrum of the deposited sample. However, careful observation indicates that the deposited sample has only peaks corresponding to anatase, as shown by "A". Peaks corresponding to rutile were not detected. The other strong peaks "B" came from the Si substrate as background. Similar spectra were obtained for the other cases. Therefore, it was confirmed that the deposited films containing nanospheres were made of anatase of titanium dioxide.

Next, the dependence of film properties on the applied voltage was examined. Figure 7 shows SEM images of the deposited film when the applied voltage was changed. In the cases of (a) 1,500 V and (b) 3,000 V, spherical nanoparticles were clearly observed. However, in the other cases of (c) 4,500 V and (d) 6,000 V, the film changed into a film without nanoparticles. It was noted that, in any case, as background, more fine structures were deposited on the Si surface, especially when  $V_d = 4,500$  V and 6,000 V, as shown in Figs. 7(c) and (d). These nanostructures might have been produced by another mechanism, which was different from that of the nanosphere formation.

The following process was considered. When the applied voltage was increased, the plasma density became large and the plasma spread outside, as shown in Fig. 2(b). As discussed in the previous paragraph, since the particles were electrically trapped near the sheath region of the plasma, those spherical nanoparticles would also be pushed outward by an expansion of the plasma in the radial direction. Therefore, the nanospheres were excluded and only a flat thin film with a fine structure remained.

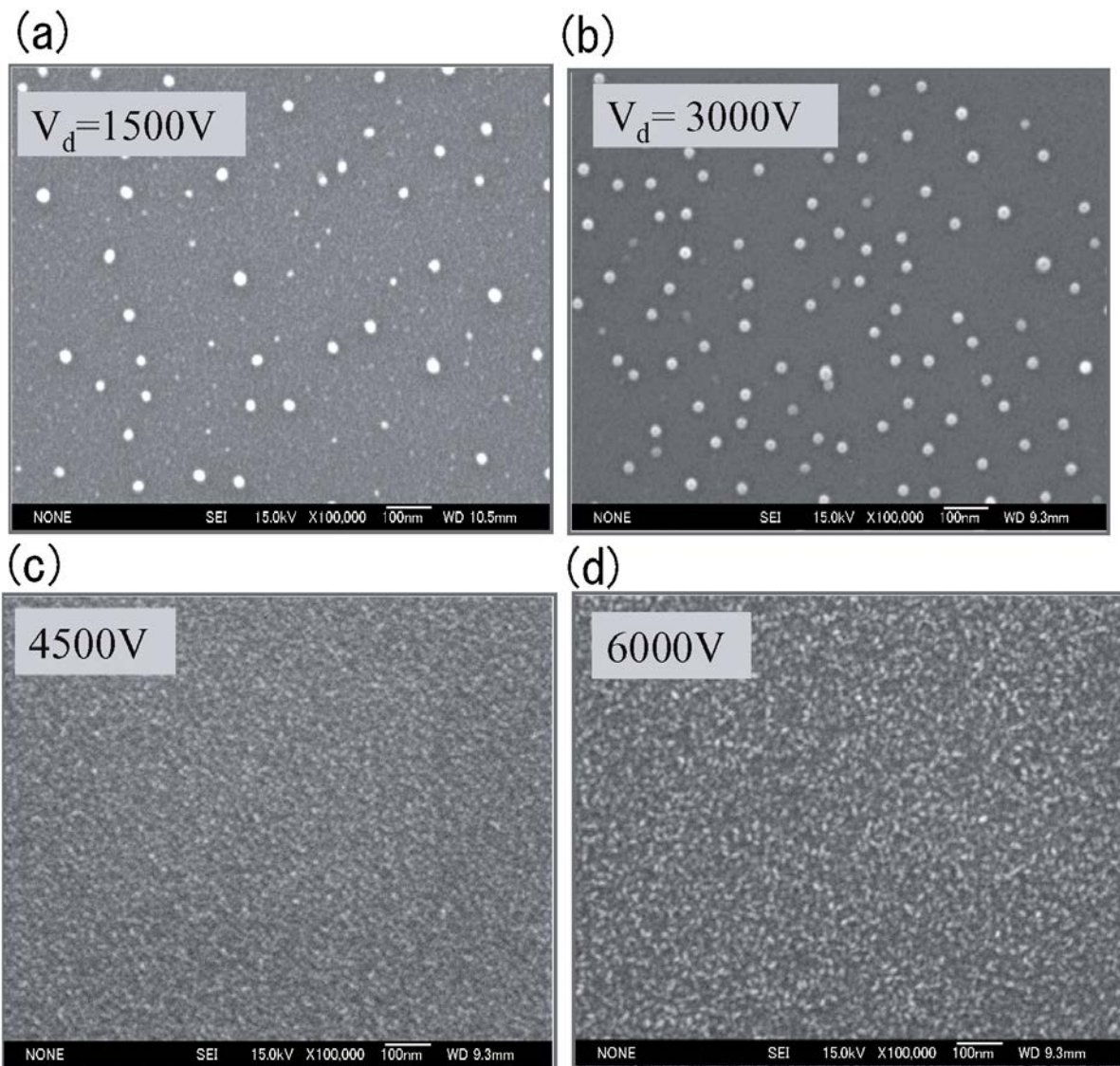


FIG. 7 SEM IMAGES OF NANOSTRUCTURES DEPOSITED ON THE SI SUBSTRATE WITH APPLIED VOLTAGE  $V_D$  AS A PARAMETER. WHEN THE APPLIED VOLTAGE WAS INCREASED, NANOSPHERES WERE OBSERVED IN THE LOW VOLTAGE CASES ((A)1,500 V AND (B)3,000 V), BUT NOT FOUND IN THE HIGH VOLTAGE CASES ((C)4,500 V AND (D)6,000 V). IN ANY CASE, AS BACKGROUND, THIN FILM WITH A FINE STRUCTURE WAS DEPOSITED.  $Ar/O_2 = 1/1$ . ALL THE MAGNIFICATIONS OF SEM IMAGES ARE 10,000 AND THE SCALE BAR IS 100 NM IN LENGTH.

In order to analyze such fine structures observed on the substrate between nanospheres, a cross-sectional TEM image of the depositions was taken, as shown in Figure 8, for the oxygen ratio of 40% and  $V_d = 1,500$  V. Many nanorods growing on the Si substrate were clearly observed in the vertical direction. Their average spacing was found to be about from 7 to 8 nm and their height was about from 30 to 40 nm. Therefore, the fine structure detected on the film surface was confirmed as that of a top view of nanorods grown tightly on the substrate in the vertical direction. It was also noted that the nanorods grew regardless of nanospheres. Therefore, the nanospheres were considered to be attached to the top of the nanorods grown on the Si substrate in the cases of  $V_d$  less than 4,500 V, as shown in Figs. 7(a)-(b).

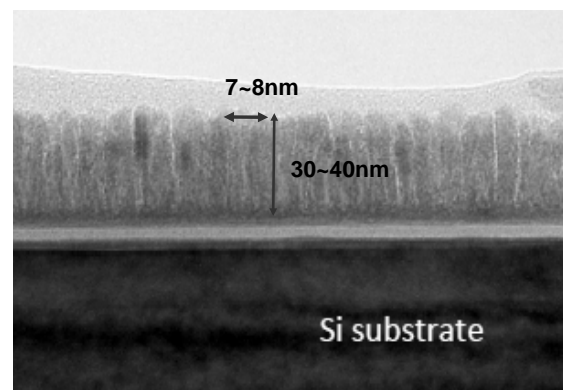


FIG. 8 CROSS-SECTIONAL TEM IMAGE OF THE FILM DEPOSITED ON THE SI SUBSTRATE. NANORODS OF TITANIUM OXIDE GREW PERPENDICULARLY FROM THE SUBSTRATE SURFACE. THEIR AVERAGE SPACING WAS ABOUT 7 - 8 NM AND THEIR HEIGHT WAS ABOUT FROM 30 TO 40 NM.  $O_2$  WAS 40%, AND  $V_D = 1,500$  V.

From these results, two mechanisms can be concluded to exist. One is a mechanism for the formation of nanospheres and the other is that for the formation of thin films with nanorods. Our results showed that nanospheres and thin film with nanorods existed simultaneously on the Si substrate.

In our previous experiment, we also observed spherical nanoparticles of MgO. According to the previous cases, the following model has been analogically considered for the formation of TiO<sub>2</sub> nanospheres and thin films with nanorods. Owing to the sheath potential in front of the Ti rod electrode, Ti atoms were sputtered by energetic Ar ions. These Ti atoms reacted with O\* atoms in the plasma to form TiO<sub>2</sub> clusters. Such seeds of TiO<sub>2</sub> nanoparticles were coagulated and grew in the plasma. Since the shape was spherical, this meant that they were grown in the discharge space without touching anywhere. If these particles were grown on the surface, their cross-sectional shape should be not a sphere but a pressed hemispherical structure.

It was speculated that the TiO<sub>2</sub> nanoclusters have been created in a space inside the glass tube, and reacted each other to form larger clusters. It was also noted that these nanoclusters have been negatively charged by the effect of electrons. Therefore, they could be confined electrically in the plasma for a long time. Owing to the ion bombardment of the ions impinging on the surface of TiO<sub>2</sub> nanoclusters levitated in the plasma, the nanoclusters would be heated up to reach a quasi-liquid state. Therefore, during growth their shape would become spherical. When these melted nanoparticles have escaped from the plasma by chance, they were immediately cooled down by collisions with neutral gases. Therefore, during solidification to form anatase, their spherical shape was reserved and such nanospheres were transported toward the substrate. Similar discussion was done for generation of spherical single crystal MgO nanoparticles with shell structure, where rise of temperature of MgO nanoparticles was estimated. Because both the specific heat and melting temperature of TiO<sub>2</sub> were lower than those of MgO, it was thought that TiO<sub>2</sub> nanoparticles could reach quasi-liquid state easier than MgO by heating of the ion bombardment in plasmas. On the other hand, Ti and O\* atoms as well as small size TiO<sub>2</sub> clusters arriving at the substrate could directly generate thin film with a finer structure composed by nanorods.

## Conclusions

An experiment on TiO<sub>2</sub> nanostructure formation was carried out under various conditions using a coaxial type electric discharge with Ar/O<sub>2</sub> mixed gas. The plasma parameters were measured and characteristic properties of the argon and oxygen plasma were clarified. It was noted that the electron temperature was decreased when oxygen was mixed in the discharge.

It became clear that titanium dioxide was generated on silicon substrates. In fact, generation of nanospheres of TiO<sub>2</sub> possibly occurred. It turned out that the diameter of nanospheres was controllable by varying the gas mixing ratio and applied voltage for the discharge. The nanospheres, grown with a size of 15 - 100 nm, were transported by a gas flow toward the substrate on which nanostructures including nanorods have grown. The crystallite was identified as anatase by Raman spectroscopy. The film quality was found to be controllable by varying the Ar/O<sub>2</sub> ratio and applied voltage.

The coaxial electrode discharge system proposed here would be quite useful for growing TiO<sub>2</sub> nanostructures including nanospheres and nanorods.

## ACKNOWLEDGMENT

This work was supported by a Grant-in-Aid for Scientific Research from The Ministry of Education, Culture, Sports, Science, and Technology, Japan.

## REFERENCES

- Chigane, M., Shinagawa, T., "Titanium dioxide thin films prepared by electrolysis from aqueous solution of titanium-lactic acid complex for dye-sensitized solar cells", *Thin Solid Films* 520 (2012): 3510-3514.
- Choi, H., Stathatos, E., Dionysiou, D., "Photocatalytic TiO<sub>2</sub> films and membranes for the development of efficient wastewater treatment and reuse systems", *Desalination* 202 (2007): 199-206.
- Feng, S., Yang, J., Liu, M., Zhu, H., Zhang, J., Li, G., Peng, J., Liu, Q., "Hydrothermal growth of double-layer TiO<sub>2</sub> nanostructure film for quantum dot sensitized solar cells", *Thin Solid Films* 520 (2012): 2745-2749.
- Dupuis, A-C., Jodin, L., Rouvière, L. E., "Catalytic growth of TiO<sub>2</sub> nanowires from a TiN thin film", *Appl. Surface Sci.* 253 (2006): 1227-1235.

- Fujishima, A., Rao, T. N., Tryk, D. A., "Titanium dioxide photocatalysis", *J. Photochem. Photobiol. C: Photochem. Rev.* 1 (2000): 1-21.
- Iizuka, S., Muraoka, T., "Single-crystal MgO hollow-nanospheres formed in RF impulse discharge plasmas", *J. Nanomaterials*, **2012**, Article ID 691874, 6 pages, doi:10.1155/2012/691874.
- Kozuka, H., Takahashi, Y., Zhao, G., Yoko, T., "Preparation and photoelectrochemical properties of porous thin films composed of submicron TiO<sub>2</sub> particles", *Thin Solid Films* 358 (2000): 172-179.
- Liu, Z. -H., Su, X. -J. , Hou, G. -L. , Bi, S. , Xiao, Z. , Jia, H. - P., "Enhanced performance for dye-sensitized solar cells based on spherical TiO<sub>2</sub> nanorod-aggregate light-scattering layer", *J. Power Sources* 218 (2012): 280-285.
- Muraoka, T., Kashimura, T., Iizuka, S., "Spherical MgO microparticle deposition by RF impulse discharge with small coaxial electrodes", *Thin Solid Films* 518 (2009): 1012-1015.
- Nishimura, G., Iizuka, S., Shimizu, T., Sato, N., "Diamond-particles levitated in a reactive plasma", *Diam. Relat. Mater.* 12 (2003): 374-377.
- Pradhan, S. S., Pradhan, S. K., Bagchi, S., Barhai, P. K., "Root growth of TiO<sub>2</sub> nanorods by sputtering", *J. Crystal Growth* 330 (2011): 1-4.
- Sanz, M., Walczak, M., Oujja, M., Cuesta, A., Castillejo, M., "Nanosecond pulsed laser deposition of TiO<sub>2</sub>: nanostructure and morphology of deposits and plasma diagnosis", *Thin Solid Films* 517 (2009): 6546-6552.

# Effect of Heat Treatment on Pitting Corrosion Resistance of Nickel Base Superalloys in Acidic Chloride Medium

Pradeep Kumar Samantaroy, Girija Suresh, U. Kamachi Mudali\*

Corrosion Science and Technology Group, Indira Gandhi Centre for Atomic Research  
Kalpakkam - 603102, India

\*kamachi@igcar.gov.in

## Abstract

Nickel base superalloys (Alloy 600, 690 and 693) were assessed by potentiodynamic anodic polarization technique for their pitting corrosion behavior in solution annealed and sensitized condition, in 3 M HNO<sub>3</sub> containing various concentrations of chloride ions, at 25°C. From the results of investigation, the solution annealed specimens showed superior pitting corrosion resistance with higher pitting potential compared to the sensitized specimens for all the alloys. Optical micrographs of the experimented specimens showed very few pits on the solution annealed specimens, where as severe pitting with grain boundary attack was observed in the sensitized specimens and the population and size of pits were found to increase with chloride ion concentration. Scanning electron microscopy study of the sensitized specimens indicated that the initiation of pits occurred in and around the grain boundary regions. Alloy 690 showed superior pitting corrosion resistance than Alloy 693 followed by Alloy 600.

## Keywords

*Superalloys; Pitting Corrosion; Polarization; Passive Film; SEM*

## Introduction

Metals and alloys which are resistant to corrosion usually depend on their ability to form and maintain a thin film of passivated oxide to protect their surface. The passive film is self-healing in nature and forms new layer whenever damage occurs on the surface. The thickness of such self-healing passive oxide layer ranges from nanometers to angstroms. However, in the influence of aggressive anions such as halides, the breakdown of such passive film occurs at weak sites on the surface. The localized anodic corrosion site is generally surrounded by a cathodic area that remains passive, which usually leads to severe pitting. Pitting corrosion is the formation of microscopic cavities on the surface of metal/alloys, due to direct corrosion of heterogeneities present on the surface or due to

localized damage causing to a protective film present on the surface. Pits are always initiated at some chemical or physical heterogeneity at the surface, such as inclusions, second phase particles, solute-segregated grain boundaries, mechanical damage, or dislocations. Pitting is considered to be autocatalytic in nature, i.e. once a pit starts to grow, the surroundings are altered such that further pit growth is promoted. Pitting corrosion resistance of various alloys are significantly affected by the metallurgical parameters, properties of chemical environment and the properties of passive film. Metallurgical parameters include alloy composition, heat treatment, cold working, sensitization, grain size, inclusions and secondary precipitates. The properties of chemical environment like pH, temperature, concentration, velocity etc. and those of the passive film like conductivity, structure, composition, capacitance etc. are known to influence pitting corrosion. From the chemical environment parameters chloride ion are the most aggressive species inducing pitting of nickel base alloys.

Nickel base superalloys form a thin, protective passive film consisting of oxides of chromium and nickel, which provides excellent corrosion resistance in variety of chemical environments. In our previous investigation, nickel base superalloys (Alloy 600, 690 and 693) were studied in the as-received condition for their pitting corrosion resistance in nitric acid-chloride medium. These alloys show high pitting potential ( $E_{pit}$ ) and good pitting corrosion resistance. Nitrate ions and chloride ions have strong opposite effect for passivation, as nitrate ion is a powerful passivating agent and chloride ion is powerful depassivating agent. The cumulative effect of these two ions can be managed by changing parameters such as alloy composition, solution composition and heat treatment. In the present investigation, Alloy 600, 690 and 693 have

TABLE 1 CHEMICAL COMPOSITION OF NI BASE SUPERALLOYS

Element	Ni	Cr	Fe	C	S	Mn	Cu	Si	Ti	Nb	N	Al	Mo
Alloy 600	74.2	14.7	9.6	0.03	0.008	0.53	0.30	0.15	0.26	-	-	0.3	0.30
Alloy 690	60	29.6	9.05	0.017	0.0013	0.21	<0.01	0.25	0.2	0.02	68 ppm	-	-
Alloy 693	60.9	29.3	3.96	0.097	0.002	0.19	<0.02	0.04	0.42	1.86	-	3.19	-

been studied for their pitting corrosion resistance under heat treated (solution annealed and sensitized) conditions in 3 M HNO<sub>3</sub> containing various concentrations of chloride ions from 500 ppm to 3000 ppm.

## Experimental

### Materials and Heat Treatment

The materials used for these investigations were Alloy 600, Alloy 690 and Alloy 693, for which the compositions are given in Table 1. The condition of heat treatment to carry out solution annealing and sensitization are tabulated in Table 2. The as-received specimens were solution annealed according to the temperature and time in Table 2 and immediately quenched in water. Solution annealing was carried out to dissolve the pre-existing carbides in the matrix. Few of the solution annealed specimens were further heat treated at the sensitization condition as per Table 2 and allowed to cool in air to induce sensitization.

TABLE 2 HEAT TREATMENT PARAMETERS

Material		Temp (°C)	Time (min)
Alloy 600	SA	1120	60
	SEN	800	60
Alloy 690	SA	1150	30
	SEN	700	60
Alloy 693	SA	1050	30
	SEN	700	60

### Specimen Preparation

Solution annealed and sensitized specimens in the dimension of 10 mm x 10 mm (exposure area approximately 1 cm<sup>2</sup>), were polished with 600 grit silicon carbide paper, mounted and then further polished up to diamond finish. The specimens were cleaned with soap solution and then with acetone. While mounting, proper care was taken to avoid gap between specimen and resin in order to prevent crevice attack during polarization experiments. These specimens were used for pitting corrosion experiments.

### Test Solution

The polarization studies were carried out in 3 M HNO<sub>3</sub> solution containing different concentrations of chloride ions (500, 1000, 2000, 3000 ppm). These solutions were prepared using reagent grade nitric

acid, sodium chloride and double distilled water.

### Pitting Corrosion Study

A three-electrode cell containing two platinum electrodes as counter electrode was used for the experiments. Heat treated nickel base superalloy (Alloy 600, 690, 693) specimens were used as working electrode. Electrochemical anodic polarization experiments were conducted in 3 M HNO<sub>3</sub> containing different concentrations (500, 1000, 2000 and 3000 ppm) of chloride ions. The specimens were allowed to stabilize at open circuit potential (OCP) for 30 minutes and subsequently subjected to potentiodynamic anodic polarization at a potential of 200 mV(SCE) below OCP, at a scan rate of 10 mV per minute under aerated conditions. The experiments were stopped beyond transpassive region where there was a monotonic increase in anodic current. All potentials were measured with reference to saturated calomel electrode (SCE) using luggin probe with the same electrolyte as the bridge. The potential at which the current increases monotonically beyond 25  $\mu$ A after the passive region was inferred as E<sub>pit</sub>. E<sub>pit</sub> is the potential above which passive alloys are susceptible to pitting corrosion, but below which pits cannot be formed, although existing pits can grow, if the applied potential is greater than the protection potential.

### Microscopy Analysis

The post experimented specimens were observed under an optical microscope to study the morphology and extent of pitting attack. Further, the specimens were observed under "SNE3000M Korea" make desktop mini-SEM, connected with EDS to locate the origin of pitting corrosion on the specimens, after electrolytic etching in 10% oxalic acid.

## Results and Discussion

The potentiodynamic anodic polarization curves for Alloy 600, 690 and 693 under heat treated (solution annealed and sensitized) conditions in 3 M HNO<sub>3</sub> medium containing various concentrations (500, 1000, 2000 and 3000 ppm) of chloride ions at room temperature are represented in Fig. 1, 2 and 3 respectively. The electrochemical parameters like corrosion potential (E<sub>corr</sub>), passivation current density

( $I_{pass}$ ) and  $E_{pit}$  are reported in Table 3.

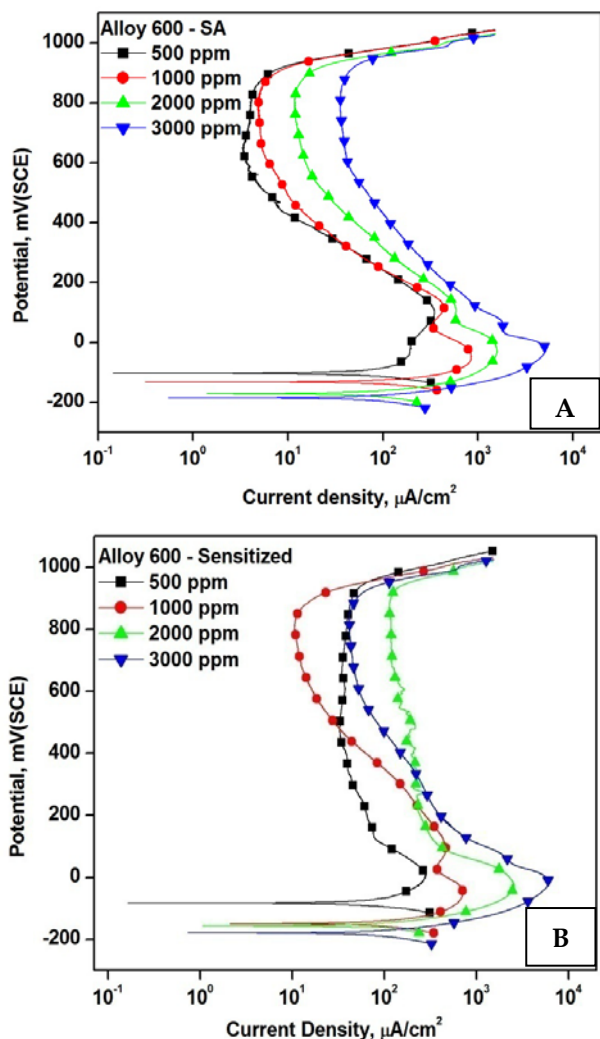


FIG. 1 POLARIZATION CURVES OF ALLOY 600 (A) SOLUTION ANNEALED (B) SENSITIZED IN 3 M HNO<sub>3</sub> CONTAINING VARIOUS CONCENTRATION OF CHLORIDE IONS

From Fig. 1, Alloy 600 (solution annealed and sensitized) showed a negative  $E_{corr}$  followed by a critical current peak during active dissolution. The active dissolution was followed by a passive region extended until oxygen evolution and then breakdown where an abrupt increase in current was recorded. The breakdown of passive film depends upon the electrode potential, environment and inhomogeneities at the surface. Breakdown of passive film results in either pitting or transpassive dissolution. For Alloy 600, the  $I_{pass}$  was found to be 3.8  $\mu\text{A}/\text{cm}^2$  for the solution annealed specimen whereas it was 35  $\mu\text{A}/\text{cm}^2$  for the sensitized specimen at 500 ppm chloride ion concentration. Further increase in chloride ion concentration caused a decrease in the  $E_{corr}$  and an increase in the  $I_{pass}$  for both solution annealed as well as sensitized specimens. Also an increase in peak current density was observed in the active region with

increase in chloride ion concentration. Pitting may occur during active dissolution, if specific regions of the specimen are more susceptible and dissolve faster than the rest of surface. For the Alloy 690 and Alloy 693 under solution annealed condition, in 3 M HNO<sub>3</sub> medium containing 500 ppm chloride ions, the  $E_{corr}$  was found in the range of 400 mV(SCE) which was found to decrease with increase in chloride ion concentration. The  $I_{pass}$  was also found to be less than 1  $\mu\text{A}/\text{cm}^2$  at all concentration of chloride ions for both the alloys. A very similar trend was observed in  $E_{corr}$  for the sensitized Alloy 690 and 693 specimens with the variation of chloride ions. The  $I_{pass}$  of sensitized Alloy 690 was found to be in the range of 1  $\mu\text{A}/\text{cm}^2$ , whereas for the sensitized Alloy 693 specimens, it was found to be in the range of 10  $\mu\text{A}/\text{cm}^2$ . The increase in  $I_{pass}$  was associated with increase in anodic dissolution. Higher value of  $I_{pass}$  could be attributed to less stability and less protective nature of the passive film.

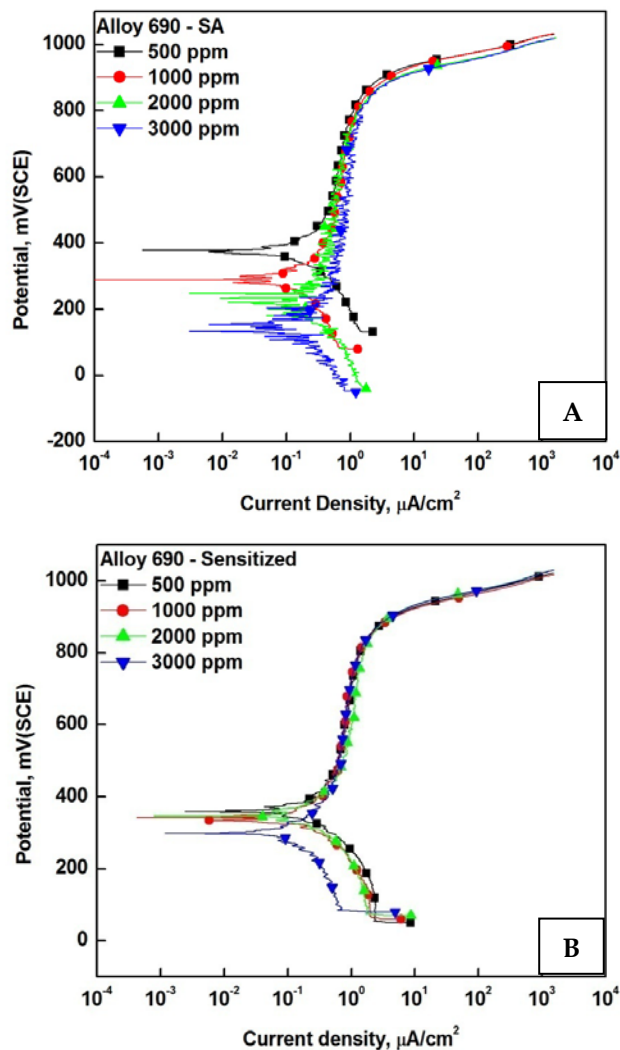


FIG. 2 POLARIZATION CURVES OF ALLOY 690 (A) SOLUTION ANNEALED (B) SENSITIZED IN 3 M HNO<sub>3</sub> CONTAINING VARIOUS CONCENTRATION OF CHLORIDE IONS

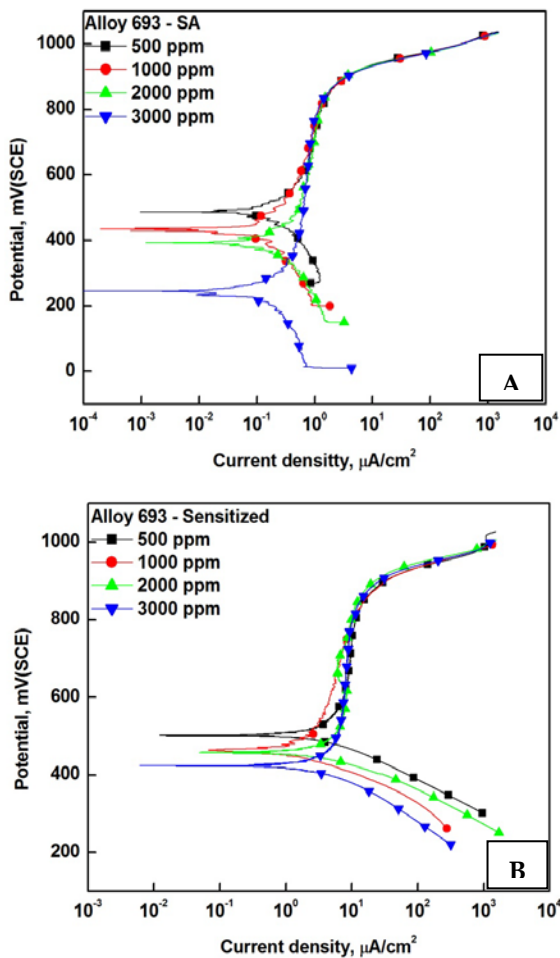


FIG. 3 POLARIZATION CURVES OF ALLOY 693 (A) SOLUTION

ANNEALED (B) SENSITIZED IN 3 M HNO<sub>3</sub> CONTAINING VARIOUS CONCENTRATION OF CHLORIDE IONS

Unlike Alloy 600, no active-passive transition was observed for the heat treated Alloy 690 and 693. Both these alloys were passivated spontaneously without any active dissolution in both solution annealed as well as in sensitized condition at all concentrations of chloride ions. The spontaneous passivation is attributed to the autocatalytic reduction of nitric acid, a mechanism which is well established.

It was observed that addition of chloride ion reduced the  $E_{corr}$  for all the alloys. This could be attributed to the fact that chloride addition promotes the anodic reaction and retards the cathodic reaction, which in turn reduces the  $E_{corr}$ . Inhibition of the cathodic reaction was a result of chloride adsorption on the surface that prevents the reduction of nitric acid to nitrous acid. According to Kolman et al, during active corrosion, the increase in anodic kinetics is greater than that in cathodic kinetics, which results in a decrease in  $E_{corr}$ . The shift of  $E_{corr}$  towards negative direction in chloride solutions indicates that the working electrode (Alloy 600) is electrochemically unstable and susceptible to anodic corrosion. Increment in chloride ion concentration promotes the active dissolution and hence a larger overpotential is required for passivation, which leads to larger peak current density.

TABLE 3 ELECTROCHEMICAL PARAMETERS OBTAINED FROM POLARIZATION CURVES

Material	Heat Treatment	Chloride Ion Conc. (ppm)	Corrosion Potential mV(SCE)	Pass. Current Density $\mu\text{A}/\text{cm}^2$	Pitting Potential mV(SCE)
Alloy 600	SA	500	-100	3.8	950
		1000	-130	5.3	950
		2000	-170	12.6	925
		3000	-185	35.9	925
	SEN	500	-85	35	920
		1000	-150	40	920
		2000	-155	42	920
		3000	-180	133	920
Alloy 690	SA	500	380	0.6	955
		1000	290	0.7	955
		2000	230	0.8	935
		3000	130	0.9	935
	SEN	500	360	0.8	950
		1000	340	0.8	950
		2000	350	0.9	945
		3000	295	0.8	950
Alloy 693	SA	500	480	0.8	955
		1000	435	0.8	955
		2000	390	0.9	950
		3000	250	0.7	950
	SEN	500	500	7	900
		1000	460	6	900
		2000	455	8	890
		3000	420	9	895

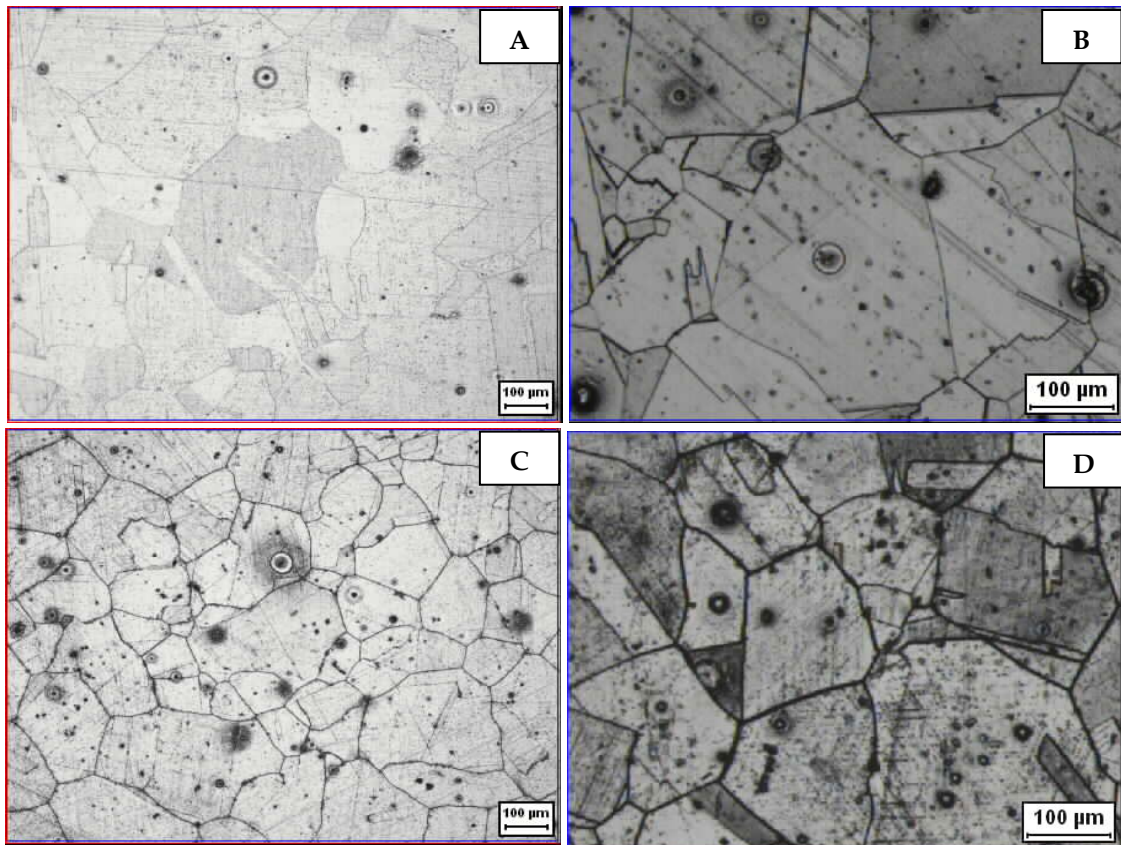


FIG. 4 OPTICAL MICROGRAPHS OF ALLOY 600 (A) SOLUTION ANNEALED IN 500 PPM (B) SOLUTION ANNEALED IN 3000 PPM (C) SENSITIZED IN 500 PPM AND (D) SENSITIZED IN 3000 PPM CHLORIDE IONS IN 3 M HNO<sub>3</sub>.

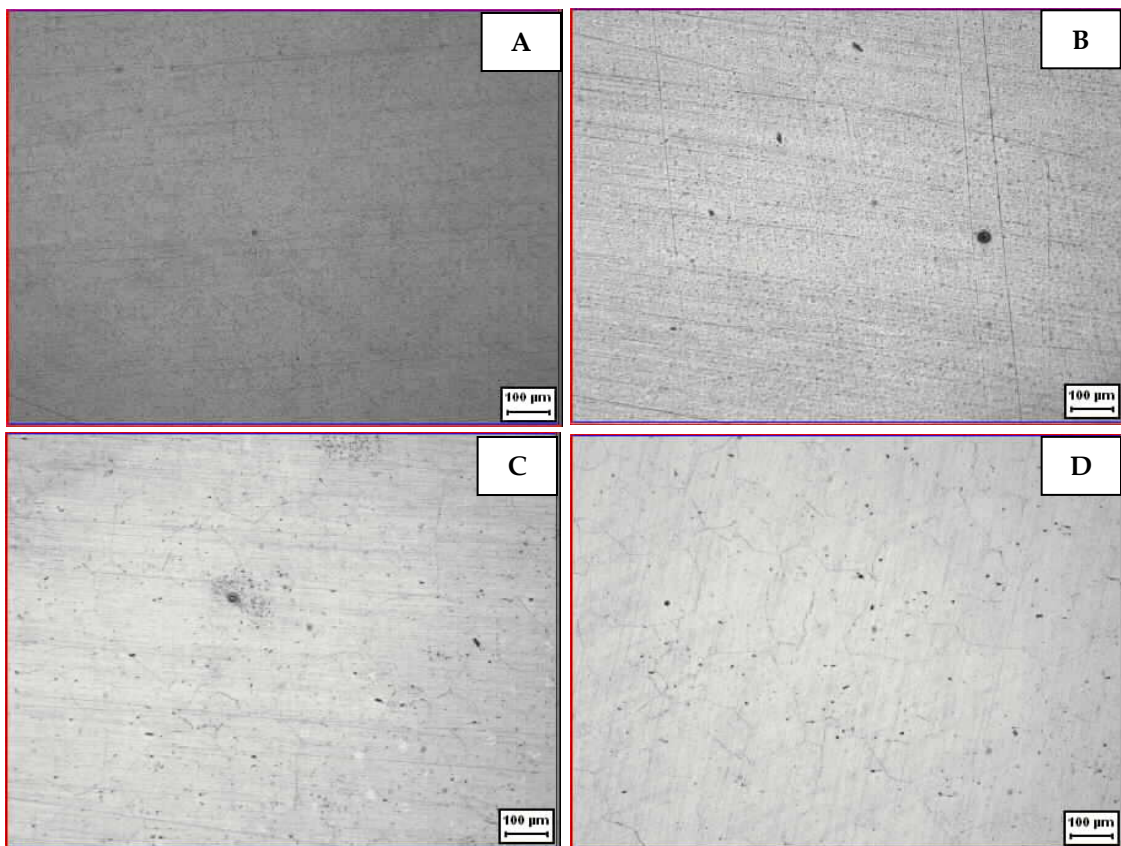


FIG. 5 OPTICAL MICROGRAPHS OF ALLOY 690 (A) SOLUTION ANNEALED IN 500 PPM (B) SOLUTION ANNEALED IN 3000 PPM (C) SENSITIZED IN 500 PPM AND (D) SENSITIZED IN 3000 PPM CHLORIDE IONS IN 3 M HNO<sub>3</sub>.

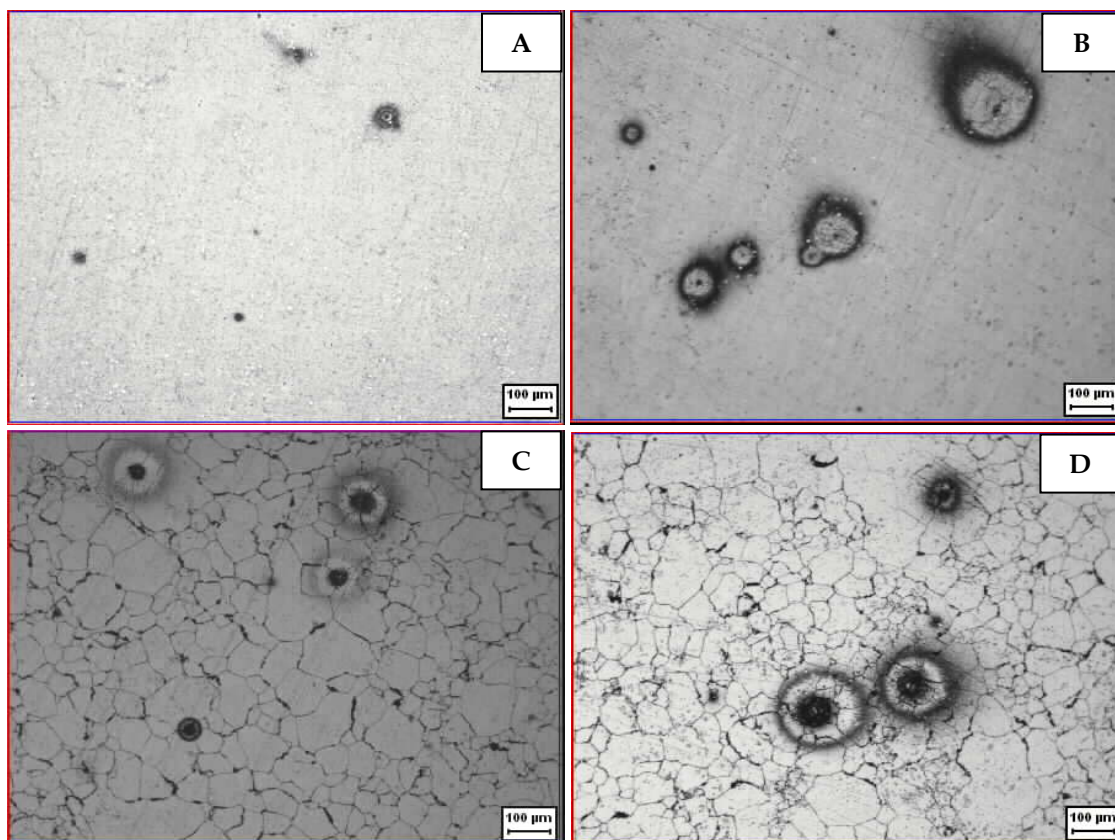


FIG. 6 OPTICAL MICROGRAPHS OF ALLOY 693 (A) SOLUTION ANNEALED IN 500 PPM (B) SOLUTION ANNEALED IN 3000 PPM (C) SENSITIZED IN 500 PPM AND (D) SENSITIZED IN 3000 PPM CHLORIDE IONS IN 3 M HNO<sub>3</sub>

Optical microscopic examination showed pit formation on all the specimens (Fig. 4-6). Alloy 690 showed only a few micropits in solution annealed condition at all concentrations of chloride ions. Whereas Alloy 600 and 693 showed pits of various sizes and shapes with attack at the grain boundaries. Also, the population and size of pits increased with increment in chloride ion concentration. In case of the sensitized specimens the grain boundaries were exposed and severe pitting was observed. Though the extent of pitting corrosion was found to be different for these alloys, the  $E_{pit}$  was found to be in the same range. All the solution annealed specimens showed  $E_{pit}$  at the range of 950 mV(SCE), whereas all the sensitized specimens showed marginally lesser  $E_{pit}$ . The observation of such high values of  $E_{pit}$  could be due to highly passivating nature of 3 M nitric acid. Many authors have investigated the corrosion behavior of different materials in solutions containing nitrate and chloride both, and reported that nitrate ions effectively inhibit pit initiation in halide solutions. Green et al have reported that nitrate ions effectively prevent pit initiation in chloride solutions, but accelerate pit growth when the nitric acid was added after pit initiation. According to Newman et al, nitrate ion has no inhibition effect on the active dissolution,

however, it passes through the salt film formed at higher potentials during diffusion controlled dissolution, causing abrupt passivation of an electrode surface. According to Ma et al the pitting inhibition of nitrate ion strongly depends on the pH of the solution. The decrease in pH is advantageous for promoting the passivation action of nitrate ions.

The passive film formed on these nickel base alloys is of oxides of Cr and Ni, reported by us elsewhere. The thickness of the passive film depends upon the experimental conditions. The presence of chloride ions may damage the film by forming  $CrCl_3$ . According to Drogowska et al, at a potentials higher than 400 mV(SCE), the oxides of Cr(III) transform to soluble  $CrO_4^{2-}$  in the presence of chloride ions and reduce the protective properties of the passive film.

The difference in pitting corrosion behavior of Alloy 600, 690 and 693 could be attributed to the differences in their chemical composition. Alloying composition and microstructure play a significant role in affecting the pitting corrosion resistance of the passive film and hence the tendency to pit. The concentration of chromium plays a dominant role in conferring passivity as its presence in any alloy is responsible for the formation of the corrosion-resistant oxide film. The

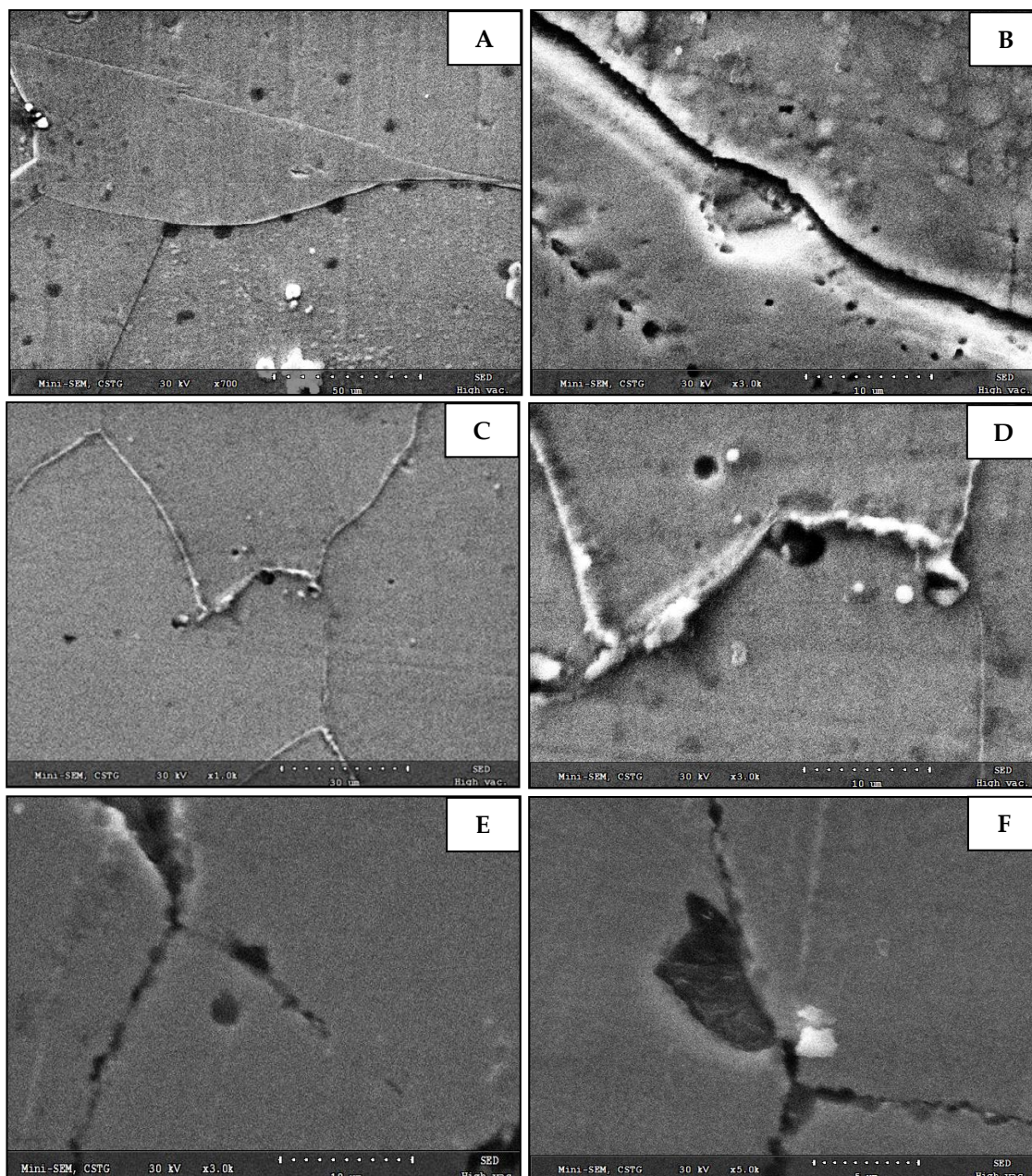


FIG. 7 SEM MICROGRAPHS SHOWING THE INITIATION OF PITS AT GRAIN BOUNDARIES (A) SOLUTION ANNEALED ALLOY 600 (B) SENSITIZED ALLOY 600 (C) SOLUTION ANNEALED ALLOY 690 (D) SENSITIZED ALLOY 690 (E) SOLUTION ANNEALED ALLOY 693 (F) SENSITIZED ALLOY 693

addition of chromium reduces the critical current density and  $I_{pass}$  and widens the passive range. The inferior pitting corrosion resistance of Alloy 600 could be attributed to the lower percentage (nearly 15%) of Cr whereas it is almost double in the case of Alloy 690 and Alloy 693. The higher concentration of manganese and sulphur also lead to more pitting in Alloy 600. The inferior pitting corrosion resistance of Alloy 693 compared to Alloy 690 could be attributed to the higher percentages of carbon (0.097%), which has resulted in carbide precipitation that provides sites prone to pitting corrosion.

Figure 7 shows the SEM images of pits formed on the

surface of various specimens. Mostly pits were found to form primarily at the grain boundaries. This could be due to the precipitation of complex carbides, which depletes this region from Cr and other alloying elements.

In the present investigation, the solution-annealed specimens were found to exhibit lower  $I_{pass}$  compared to the sensitized specimens, for all the alloys. This could be attributed to the stable passive film formation on the surface of solution-annealed specimen as a result of homogenized microstructure. Solution treatment at high temperatures helps in dissolving second phase particles, which leads to marked

improvement in pitting resistance. A stable passive film formed on the solution-annealed specimen has resulted in improved corrosion resistance when compared to the sensitized specimens.

## Conclusions

The following conclusions could be drawn based on the results of the present investigation on the effect of heat treatment on the pitting corrosion behavior of Alloy 600, Alloy 690 and Alloy 693 in 3 M HNO<sub>3</sub> contain various concentrations (500, 1000, 2000 and 3000 ppm) of chloride ions:

- (a) With the increase in chloride ions concentration in the acidic chloride medium, the  $E_{corr}$  was found to decrease.
- (b) All the alloys showed high  $E_{pit}$ , which could be due to presence of nitrate ions. Nitrates ions inhibit the pitting initiation in these alloys in chloride containing medium.
- (c) Alloy 600 was found to show inferior corrosion resistance as compared to Alloy 690 and Alloy 693, which could be due to lower concentration of Cr in the alloy. With increase in chloride ion concentration, the pitting attack was found to increase for all the alloys.
- (d) The solution annealed specimen was found to show superior pitting corrosion resistance as compared to sensitized specimens for all the alloys, which could be due to homogenized microstructure.

## ACKNOWLEDGMENT

The authors acknowledged Mr. T. Nandakumar of Corrosion Science & Technology Group, IGCAR for the technical support in carrying out the specimen preparation and the polarization tests.

## REFERENCES

- Asami A., Hasimoto K., Shimodaira S., Corros. Sci. 18 (1978): 151.
- Balboud F., Sanchez G., Fauvet P., Santarini G., Picard G., Corros. Sci. 42 (2000): 1685.
- Burstein G. T., Nature 350 (1991): 188.
- Chang M. Y., Yu G. P., J. Nucl. Mater. 202 (1993): 145.
- Drogowska M., Menard H., Brossard L., J. Appl. Electrochem. 26 (1996): 491.
- Drogowska M., Brossard L., Menard H., J. Appl. Electrochem. 28 (1998): 491.
- Fauvet P., Balbaud F., Robin R., Tran Q. T., Mugnier A., Espinoux D., J. Nucl. Mater. 375 (2008): 52.
- Frankel G. S., J. Electrochem. Soc. 145 (1998): 2186.
- Girija S., Kamachi Mudali U., Shankar V., Dayal R. K., Trans. Ind. Inst. Met. 55 (2002): 439.
- Girija S., Raju V. R., Kamachi Mudali U., Dayal R. K., Corros. Eng. Sci. Tech. 38 (2003): 309.
- Green N. D., Fontana M. G., Corrosion 15 (1959): 32t.
- Hickling J., Wieling N., Corrosion 37 (1981): 147.
- Kamachi Mudali U., and Pujar M. G., Corrosion of Austenitic Stainless Steels - Mechanism, Mitigation and Monitoring, Edited by Khatak H. S., and Raj B., Narosa Publications (2002), 74.
- Kamachi Mudali U., Dayal R. K., Gnanamoorthy J. B., Rodriguez P., ISIJ Int. 36 (1996): 799.
- Kamachi Mudali U., Shankar P., Ningshen S., Dayal R. K., Khatak H. S., Raj B., Corros. Sci. 44 (2002): 2183.
- Kolman D. G., Fort D. K., Butt D. P., Nelson T. O., Corros. Sci. 39 (1997): 2067.
- Kolotykin Y. M., Corrosion 19 (1963): 261.
- Lumsden J B, In Proc Int Conf Corrosion of Nickel Base Alloys, ASM, Cincinnati, OH (1985), 181.
- Ma H. C., Yang C., Li G. Y., Guo W. J., Chen S. H., Luo J. L., Corrosion 59 (2003): 1112.
- Mazza B., Pedferri P., Sinigaglia D., Cigada A., Mondora G. A., Re G., Taccani G., Wenger D., J. Electrochem. Soc. 126 (1979): 2075.
- Newman R. C., Ajjawi M. A. A., Corros Sci 12 (1986): 1057.
- Ningshen S., Kamachi Mudali U., J. Mater. Eng. Perform. 19 (2010): 274.
- Palumbo G., King P. J., Aust K. T., Corrosion 43 (1987): 37.
- Rarey C. R., Aronson A. H., Corrosion 28 (1972): 255.
- Samantaroy P. K., Girija S., Kamachi Mudali U., Corrosion 68 (2012): 046001-1.
- Samantaroy P. K., Girija S., Krishna N. G., Kamachi Mudali U., J. Mater. Eng. Perform. 22 (2013): 1041.
- Samantaroy P. K., Girija S., Paul R., Kamachi Mudali U., Raj B., J. Nucl. Mater. 418 (2011): 27.
- Schwenk W., Corrosion 20 (1964): 129t.
- Sedriks A. J., Corrosion of Stainless Steels, John-Wiley and Sons, New York (1996).
- Sedriks A J, In: Proc Int Conf Stainless Steels-85, The Institute of Metals, London (1985), 125.
- Semino C. J., Pedferri P., Burstein G. T., Hoar T. P., Corros.

- Sci. 19 (1979): 1069.
- Singh I. B., Corrosion, 57 (2001): 483.
- Stefec R., Franz F., Holecek A., Werkst. Korro. 30 (1979): 189.
- Szklarska-Smialowska Z., Corrosion 27 (1971): 223.
- Szklarska-Smialowska Z., Corros. Sci. 18 (1978): 97.
- Szklarska-Smialowska Z., Pitting Corrosion of Metals, NACE, Houston, TX (1986) p 144.
- Tomashov N. D., Tehernova G. P., Mankova N., Corrosion 20 (1964): 166t.
- Tomashov N. D., Cherrnova G. P., Rutten M. Y., Prot. Met. 18 (1982): 671.
- Uligh H. H., Gilman J. R., Corrosion 20 (1964) 289t.